University of Bremen

Faculty 1: Faculty of Physics and Electrical Engineering

Master of Science in Environmental Physics

Upper-ocean turbulence and mixing in the southern Atlantic

Master's Thesis by

Letizia Roscelli

Matriculation Number: 6024027

Supervisor:
   Dr. Christian Mertens

Second Supervisor:
   Prof. Dr. Torsten Kanzow

Submission date: 17th January 2023

Winter Semester 2022/2023

Abstract

Internal waves in the ocean propagate over large distances and, when they break, cause energy dissipation through mixing in turbulent patches. A parameterization of diapycnal mixing is necessary in order for both internal waves and small scale turbulence to be accounted for in ocean and climate models. The data analyzed in this thesis were collected with a Vertical Microstructure Profiler during some in situ observations in the region located southeast of the Walvis Ridge, in the eastern South Atlantic. Energy dissipation rate and diffusivity profiles collected at different locations all show similar trends and comparable magnitudes. The same is true for the depth (from 100 to 600 meters) integrated energy dissipation. A key result is that $84\% \pm 9\%$ of the dissipation in a vertical profile is caused by the smallest detectable scales and not by notable turbulent events. Estimates of the energy dissipation directly obtained from shear microstructure profiles were also compared with indirect estimates calculated from density finestructure measured with a Conductivity-Temperature sensor. Vertical inversions in oceanic water density are, in fact, commonly used to calculate energy dissipation rates, assuming a statistically valid linear scaling between the Thorpe scales and the Ozmidov scales. Much attention was paid here to accurately calculate reliable Thorpe scales from density inversions, following some methodological papers, applying several corrections including the reduction of the effects of density noise by computation of an intermediate density profile, and overturn verification through the overturning ratio parameter. The so obtained, averaged, turbulent energy dissipation rate profiles were satisfying and encourage the idea of routinely calculating Thorpe scales from CTD measurements to provide information on spatial locations and time variability of significant shear-generated mixing. Another set of data was also analyzed, collected in the same area using a MicroRider mounted on a Glider, but an appropriate comparison between the two datasets would require further processing and study.

Contents

1 Introduction

In the ocean, there is a continuous transfer of energy from the identifiable currents (the mean flow) to eventual dissipation as heat. This occurs via a succession of eddies, i.e. meanders and rings of water, of generally decreasing size. Therefore, a "cascade" of energy transfer takes place: from large-scale features down to smaller and smaller eddies (even a few centimetres across or less), down to the molecular level. Fluids, such as water, are highly turbulent, which means that they are not very viscous. Turbulent mixing of water with different densities that occurs across isopycnal surfaces (i.e. surfaces of constant density) is referred to as "diapycnal mixing".

In order to understand turbulence, it is important to resolve energy-containing scales and the stratification background against which overturns work. Energy-containing scales vary from centimetres, in the upper pycnocline, to tens of meters, in the abyss. The pycnocline separates the weakly stratified interior from the surface boundary layer and usually begins tens of meters below the ocean surface. At the base of the surface layer, the stratification peaks. Below that, the density gradient decreases with increasing depth, until it smoothly merges into the weakly stratified abyss. Kinetic energy is converted to heat, that is internal energy, by molecular friction at the end of the small-scale turbulent kinetic energy cascade [Eden et al. (2014)]. Such dissipation involves enhanced molecular mixing of temperature and salinity, hence, mixing of density. One of the drivers of the meridional overturning circulation, the circulation in the ocean at the largest scale, is, indeed, this density mixing [Munk (1966)].

Microstructure refers to the signatures of oceanic turbulence at scales smaller than 1 m, usually of the order of 1 cm, where molecular viscosity and diffusion are important. Viscosity dissipates the turbulence and enhances heat and salt diffusion by straining their mean gradients until diffusion smooths them [Gregg (2021)]. Microstructure profile measurements are the basis for quantifying mixing, but they are too spatially and temporally limited to appropriately cover the entire ocean.

Interactions between the different dynamical regimes in the ocean transfer large amounts of kinetic and potential energy and dissipate the energy input into the ocean by tidal and atmospheric forcing. An important component of the energy cycle of

the ocean is the internal wave field, which links over large distances different energy sources for mixing and dissipation. Internal waves, also called gravity waves, are mostly generated at the sea surface by wind and at the seafloor by currents over rough topography. While propagating from the boundaries into the ocean interior, they transport energy in all directions and transfer it to smaller scales through the nonlinear wave–wave interaction within the internal gravity wave field. The resulting shear or convective instability, i.e. the reflection or breaking of internal waves, for example at the shelf break, causes mixing of the water column and is an important source of turbulence and energy dissipation in the ocean interior (e.g. Munk (1981)). Internal waves and small-scale turbulence are two regimes that play an essential role in the energy cycle of the ocean [Eden et al. (2014)]. Yet, many parts of these processes, in particular shear instability and dissipation, are unresolved in ocean circulation models. This is due to the unsuitable resolution caused by large differences in their temporal and spatial scales (see Fig. 1).
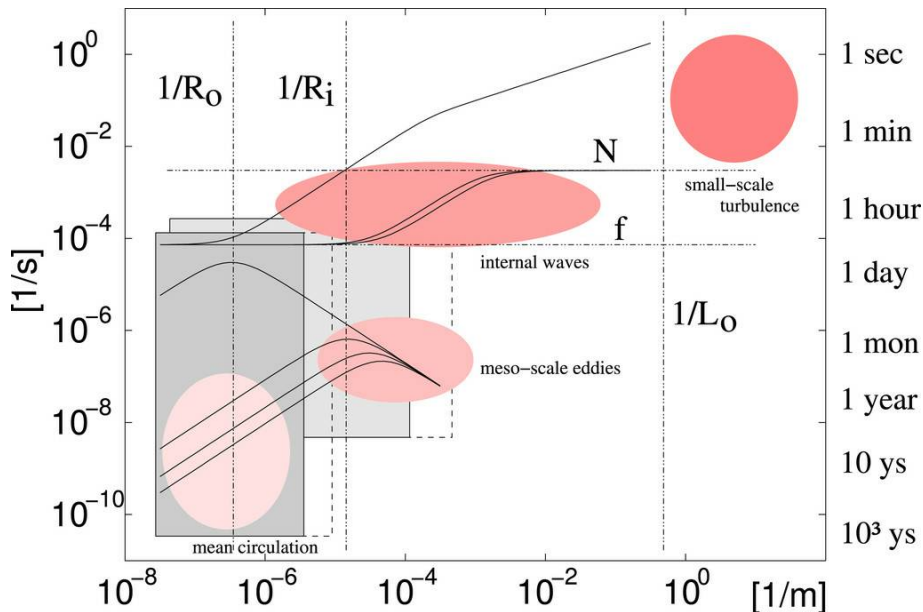
Figure 1: Simplified graphic representation of different dynamical regimes in the ocean as a function of wavenumber and frequency. The Ozmidov scale L_O separates small-scale turbulence and waves. R_i and R_o are the internal and the barotropic Rossby radius, respectively. Source: From Eden et al. (2014).

In order for models to include both small-scale turbulence and internal waves, a parametrization of such phenomena is needed. Observations are complicated by turbulence small scales and intermittency, but they are the key to a better under-

standing and description of such processes.

The data sets used in this thesis were collected in March and April 2022 during the M180 SONNET (Synoptic Observations - a Nested approach to study Energy Transfer & Turbulence in the ocean) expedition, which was part of the observational program of the second phase of TRR 181 "Energy Transfers in Atmosphere and Ocean". The expedition took place southeast of the Walvis Ridge in the eastern South Atlantic (see Fig. 2 for a panoramic view of the entire cruise path and Fig. 3 for an overview of the stations' positions), an ocean region where it is possible to observe numerous processes that affect energy fluxes in the ocean and its exchange with the atmosphere.
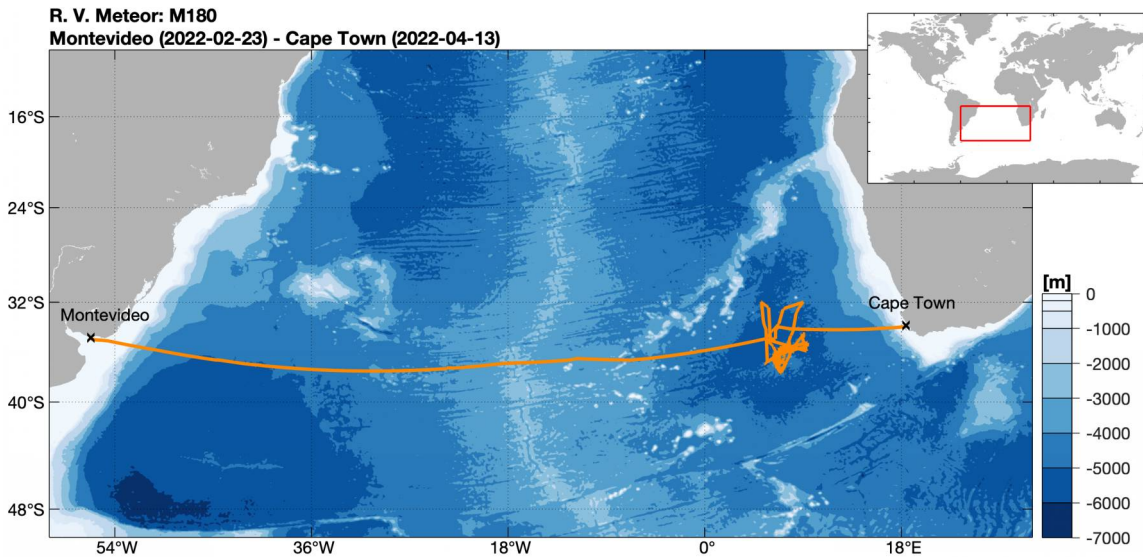
Figure 2: Map with the complete track followed by the research vessel Meteor during the SONNET expedition in the South Atlantic Ocean. Source: M. Walter, personal communication.

The so-called Agulhas rings are eddies that form to the south of the African continent from the Agulhas Current looping back on itself, and are an important agent in the transfer of water and heat between the Indian and Atlantic Oceans. These highly energetic ring-like eddies migrate north-westwards through the Atlantic Ocean and meet internal tides generated at the Walvis Ridge. The propagation of internal tidal waves is, hence, affected, and fronts and filaments are formed at the eddies' edges. Therefore, the studied region combines features that appear to be very interesting when studying energy propagation, transmission, and dissipation: warm centered eddies that enter the Atlantic coming from the Indian Ocean and an ocean ridge. An ocean ridge is a continuous range of underwater volcanoes formed by plate

tectonics, along divergent plate boundaries, where new ocean floor is created as the Earth's tectonic plates spread apart. Ridges stand out clearly above the background bathymetry, thereby affecting circulation. The Walvis Ridge, for example, blocks direct northward flow into the eastern South Atlantic from the south. Therefore, the aim of the expedition was to better understand the processes taking in that area, and characterize the energy cycle and its balance in this ocean region.
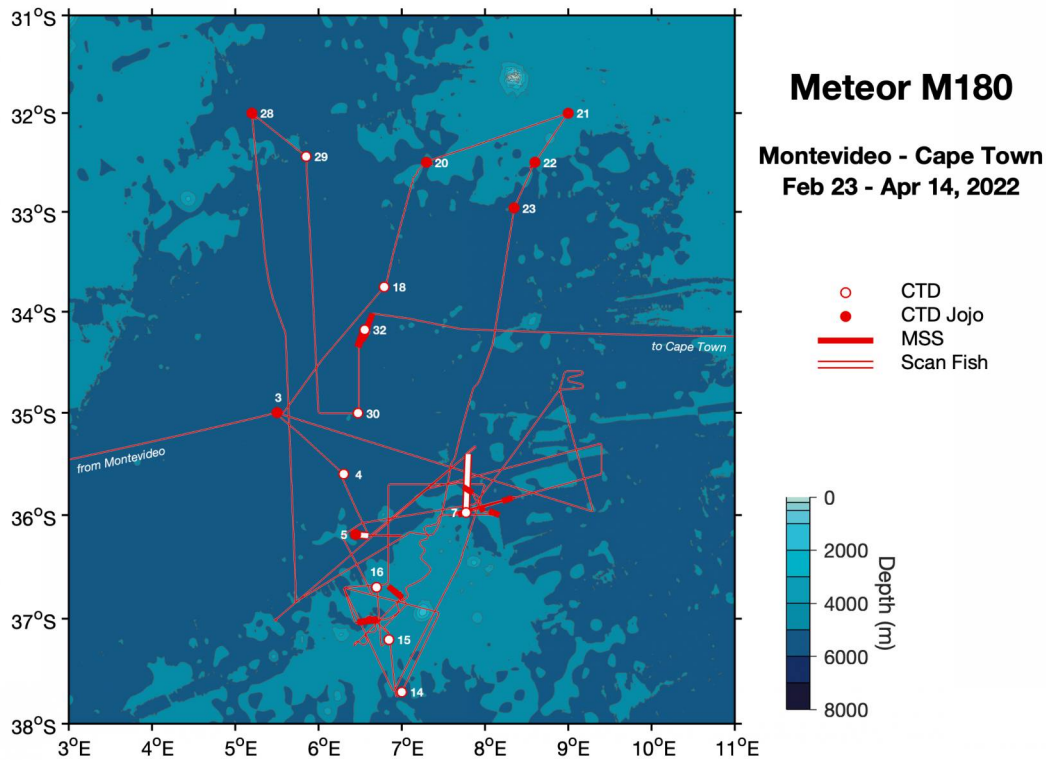
Figure 3: Map with the location of all the stations where measurements were performed during the SONNET expedition. Source: M. Walter, personal communication.

Two oceanic data sets were analyzed, both collected during the SONNET cruise. The first data set was measured deploying a Vertical Microstructure Profiler (VMP) at eleven different stations. The second data set was obtained with a Microrider (MR) that was mounted on a Glider and operated for around 8 days, from the 16th to the 24th of March 2022.

The purpose of this thesis is, hence, to study energy dissipation rate estimates in the eastern Southern Atlantic, next to the Walvis Ridge, and to give an overview of relevant information obtained from the analysis of the data collected with the VMP and the MR during the SONNET cruise.

From both the processed data sets, it is possible to obtain direct estimations of the energy dissipation rate, ε. When using dissipation-scale sensors, such as those featured in Vertical Microstructure Profilers and Microriders, ε is estimated from spectra taken over windows of one-half to several meters. Spectra are corrected with probe response functions, integrated, and scaled. The underlying assumption is that gradients are isotropic, which means that they are the same in all directions. For each VMP cast, the profiles of numerous variables were computed, such as density ρ, turbulent (a.k.a. eddy) diffusivity K_ρ, and depth integrated energy dissipation rate ϵ. All these parameters are of great interest when studying the ocean from an energetic point of view. For example, small-scale mixing is proportional to turbulent diffusivities. Also, the potential presence of regional differences in the measured dissipation was evaluated. In particular, it was investigated whether the results showed any remarkable difference between the dissipation rate estimates obtained in the three subareas in which the study area of the SONNET cruise was divided (see Fig. 4), each one corresponding to a specific oceanic regime: the Tidal Beam Study Region (BEAM), the Eddy Study Region (EDDY), and the Submesoscale Study Region ((S)MESO). These are shown in Fig. 4.

From the data collected with the VMP, not only the energy dissipation rates directly estimated from microstructures (ε) were obtained, but also some energy dissipation estimates inferred from largest turbulent scales using Thorpe Scale (ε_T). The Thorpe Scale (L_T), introduced by Thorpe (1977), is a measure of the vertical length scale of water parcels' overturns that, in a stratified fluid, are related to gravitational instabilities [Ferron et al. (1998)]. Overturns can be identified by looking for density or temperature inversions in the measured profiles. The fact that the very local density, and often temperature, inversions in the ocean interior are accompanied by intense microstructure has been used by many studies (e.g. Ferron et al. (1998)). On the other hand, microstructure ensembles have been used to validate mixing estimates from density overturns (e.g. Dillon (1982)) and from finestructure variances of shear and strain over vertical scales from tens to a few hundred meters (e.g. Gregg (1989)). The advantage of estimating energy dissipation rates from Thorpe Scale is that, in order to apply this method, simple conductivity-temperature-depth (CTD) profiles are needed. CTD casts are very numerous and widely distributed,

especially compared to VMP casts, saving time and money. However, some precautions and corrections must necessarily be applied, if one hopes to obtain reliable estimates. Therefore, it is of our interest to investigate the agreement between different dissipation estimates (namely ε and ε_T), evaluate their relationship, and find potential problems of the two methods. Finally, similarities and differences between ε estimates from VMP measures and from MR measures were investigated within an area where both VMP and MR casts were available.

This Master's thesis paper is structured as follows: in section 2 the scientific background is introduced, in section 3 the methods used for the data collection first and the data analysis then are described. The results are presented in section 4 and discussed in section 5, together with some other considerations and evaluations. Finally, section 6 contains a brief summary of the work done and the conclusions.
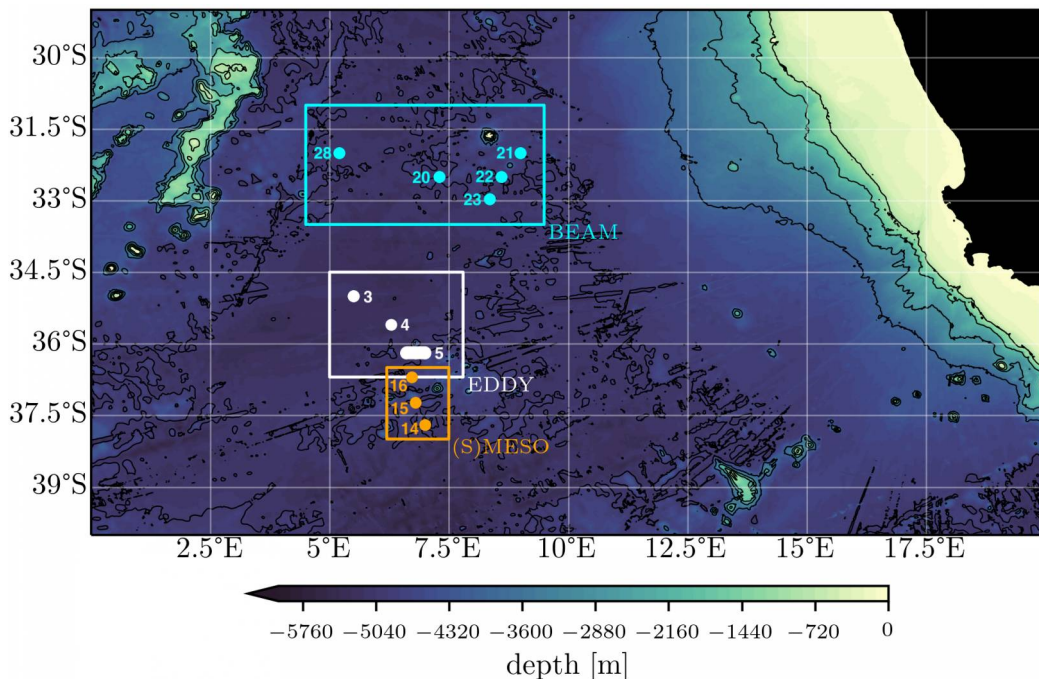
Figure 4: Map of the Southern Atlantic Ocean where the measures of the SONNET scientific cruise took place, with the ocean bathymetry. The black shape on the right side is the African continent. The stations in which vertical microstructure measures were carried out are pointed by the dots, and the corresponding station numbers are shown. The stations are inside boxes that indicate the different study areas: Tidal Beam Study Region (BEAM), Eddy Study Region (EDDY), and Submesoscale Study Region ((S)MESO). Station 5 looks elongated because the deployments of the different blocks of casts of that station were not carried out at the exact same longitude. [Simon Reifenberg, 2021, personal communication]

2 Scientific Background

2.1 Turbulence and Mixing

Water *mixing* in the ocean is often a general term. It can include phenomena that take place at large length scales, but it is also not complete until molecular viscosity smooths velocity fluctuations to remove significant shear. A complete description of all the processes involved is given by Gregg (2021) and summarized here.

A fundamental parameter when studying mixing is the viscous dissipation rate [W kg^{-1}]:

$$\varepsilon \equiv \nu(\overline{\nabla \boldsymbol{v}'})^2 \tag{1}$$

since it represents the flux of energy from large to small scales when turbulence is at steady state. In Eq. 1, ν is the kinematic viscosity of seawater, and $\boldsymbol{v}'$ is the vector of water velocity fluctuations.

Density fluctuations correlated with vertical velocity produce vertical fluxes of density (buoyancy fluxes) that affect dynamics. These diapycnal velocities (velocity across an isopycnal surface) are proportional to vertical divergences of the buoyancy fluxes. Available potential energy (ape) that destabilizes stratification is created and when the instability collapses, it generates turbulent kinetic energy (tke). Tke is eventually converted into potential energy by diffusion and into heat by molecular viscosity at rate ε through frictional interaction with the sea-bed or internal friction.

Turbulence occurs episodically in thin, intermittent patches. Some sequential depth intervals show high turbulence, while others varying amounts. Probability densities of these ensembles are highly skewed and roughly lognormal [Gregg (2021)]. To study turbulence at small scales and its impact on the larger scales of interest, fluid dynamicists introduced the concept of turbulent, or eddy, diffusivity, in which turbulent "eddies" at smaller scales accomplish the diffusion. Eddy diffusivity is much higher than molecular diffusivity since turbulent eddies carry properties much farther than molecular motions. While molecular diffusivities only depend on the temperature, salinity, and pressure of the water, eddy diffusivities also depend on the intensity and structure of the turbulence. Currently, the diapycnal eddy coefficient for density, K_ρ [m^{2}s^{-1}], is estimated from microstructure by assuming that the average rate of turbulent kinetic energy production balances the average rate of its

dissipation by viscosity or by scalar diffusion:

$$K_\rho = \Gamma_{mix}\varepsilon/N^2 \qquad (2)$$

with Γ_{mix} as the mixing coefficient, a measure of the efficiency of stratified turbulence, and N as the buoyancy frequency. Mixing efficiency is defined as the increase in reference, or background, potential energy divided by the energy expended to produce the mixing,

$$\text{mixing efficiency} \equiv \frac{\Delta gpe_r}{\text{energy expected to produce the mixing}} \qquad (3)$$

where Δgpe_r is the increase in reference gravitational potential energy produced by the mixing. There are many variations of the variables used to evaluate efficiency [Gregg et al. (2018)], but here we used the value for the mixing coefficient that is widely reported from oceanic measurements: 0.2. Munk (1966) obtained a globally averaged vertical eddy diffusivity K_ρ of 10^{-4} m^2 s^{-1}, accounting for the observed average vertical density structure. However, the directly observed vertical (or diapycnal) eddy diffusivity in most of the ocean is one order of magnitude lower: $K_\rho \sim 10^{-5}$ m^2 s^{-1} [Gregg and Sanford (1988)], implying that there are regions of much higher diffusivity to reach the global average. Measurements show huge enhancements of diapycnal eddy diffusivity K_ρ in bottom boundary regions, especially where topography is rough [Polzin et al. (1997)], and on continental shelves where tidal energy is focused [Lien and Gregg (2001)].

2.2   Eddies and Agulhas Rings

Flow in the oceans is turbulent, and isopycnal mixing predominantly results from the "stirring" by turbulent eddies, which form because flowing water has a natural tendency to be turbulent and chaotic. The following description is a summary of Chapter 3.5.2 from Brown et al. (2001). Eddies of various sizes are generated by interaction of currents with the bottom topography, islands, coasts, or other currents or eddies, or as a result of horizontal wind shear. Spatial variations in flow velocity (i.e. horizontal or vertical current shear) cause small disturbances or perturbations in the flow to grow, developing into wave-like patterns and/or eddies. These effects are defined as non-linear because they can not be predicted simply by adding together

flow velocities. The ocean is full of eddies and they contain a significant proportion of the ocean's energy. Although eddies occur over a wide range of space- and time-scales, mesoscale (which means "intermediate scale") eddies dominate variable flows with periods greater than the tidal and inertial periods. Mesoscale eddies are an intrinsic part of the ocean circulation. They generally have length scales of 50-200 km, periods of one to a few months, travel at a few kilometres per day, and have rotatory currents with speeds of the order of 0.1 m s^{-1}. In most mesoscale eddies, but not all, flow is in approximate geostrophic equilibrium. They are known to form from meanders in intense frontal regions, such as the Gulf Stream and the Antarctic Circumpolar Current, but may form in other ways too.

A good introduction to Agulhas rings is given in Talley et al. (2011) and summarised here. Agulhas rings are large, anticyclonic (i.e. rotating counterclockwise) eddies of warm surface water from the Indian Ocean that move northwestward into the South Atlantic Ocean.
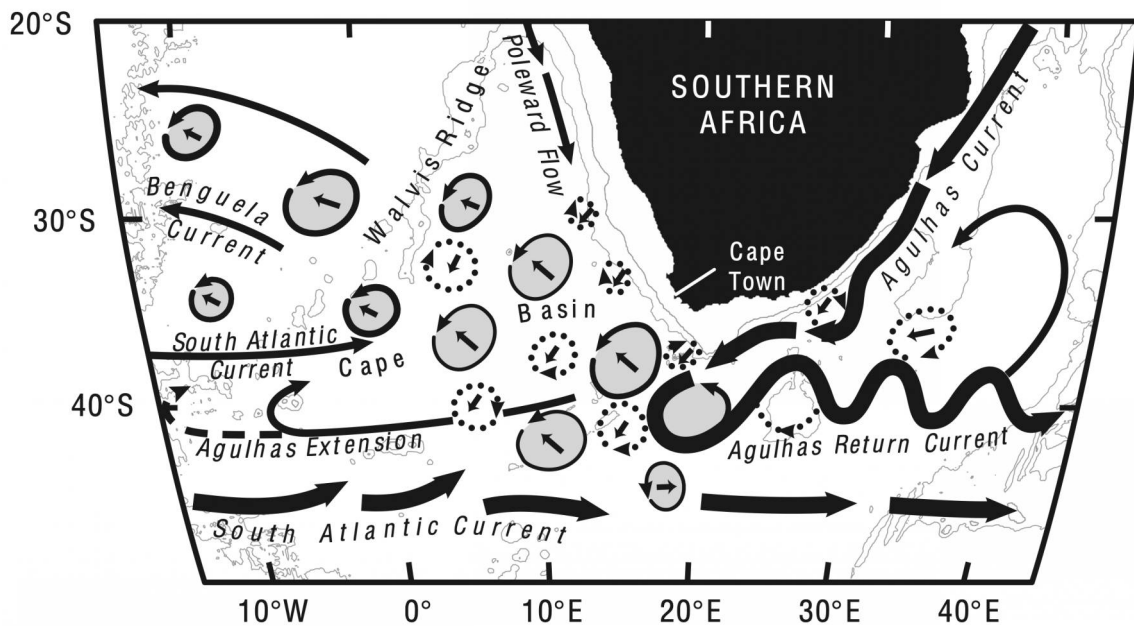
Figure 5: Schematic map of the Agulhas Current, retroflection, and eddies. Gray-shaded rings are the Agulhas anticyclones rings that populate Cape Basin. Dashed rings are cyclones, many of which form along the northern boundary of the Agulhas Current, south of Africa. Source: From Richardson (2007).

They generate at the southern tip of Africa, where the Agulhas Current rounds, between 15°E and 20°E. The Agulhas Current (Fig. 5) is the western boundary

current of the Indian Ocean's subtropical gyre. It is narrow, swift, and one of the strongest currents in the global ocean. The Agulhas follows the continental shelf to where it ends at about 36°S and then separates from the African coast. It overshoots into the South Atlantic and then most of it retroflects back into the Indian Ocean, turning abruptly eastward. It sheds large rings at the retroflection that propagate westward into the South Atlantic. The centers of the Agulhas rings are warm and saline in contrast with the local South Atlantic waters. The rings are 100-400 km in diameter, with maximum speeds of more than 1 m s^{-1} at the surface, and up to 0.1 m s^{-1} even at 4000 m depth.

2.3   Internal Waves

Turbulence produces fluctuations in temperature and salinity. These fluctuations occur on microstructure length scales, the smallest of physical significance in the ocean. Two processes produce nearly all microstructure in the ocean interior: double diffusion and internal waves [Gregg (2021)]. The following introduction to internal waves is a summary of the overviews provided by Wright et al. (1999) and Talley et al. (2011). Internal gravity waves, or internal waves, are three dimensional waves occurring at interfaces between oceanic water layers of differing densities. These occur most commonly where there is a steep density gradient, that means steep gradients of temperature and/or salinity, the two properties which together govern the density of seawater. Internal waves are mostly generated by barotropic tides interacting with sloping topography, by wind stirring the mixed layer, and by geostrophic flows over rough terrain, which usually generates internal waves with frequencies close to the Coriolis frequency f. The Coriolis frequency, f, and the buoyancy frequency, N, bound the range of possible frequencies for internal waves (ω_{in}).

The stratification in the ocean interior is much weaker than between the ocean and the atmosphere. Hence, the restoring force (the buoyancy force, which is due to heat and freshwater fluxes) is weaker because displacing the interface from its equilibrium position requires less energy. Therefore, oscillations are more easily set up between oceanic water layers than at the sea-surface, and internal waves have often greater amplitudes compared to surface waves (few tens of meters, up to 100 m), longer periods (minutes or hours rather than seconds) and longer wavelengths

(hundreds rather than tens of metres).

Waves, including internal waves, possess both kinetic and potential energy. Kinetic energy is the energy inherent in the orbital motion of the water particles, whereas potential energy is the energy that particles possess as a result of being displaced from their mean (equilibrium) position. For a water particle in a given wave, energy is continually being converted from potential energy (at crest and trough) to kinetic energy (as it passes through the equilibrium position), and vice versa. The potential energy of the world ocean is about one hundred times greater than its kinetic energy [Brown et al. (2001)]. The speed of ocean currents does not increase dramatically because an equilibrium has been reached whereby the rate at which energy is supplied is being balanced by the rate at which it is being dissipated. The dissipation of energy takes place in four main ways: white-capping, viscous attenuation (only important for very high frequency capillary waves, involves energy being dissipated into heat by friction between water molecules), air resistance, and non-linear wave-wave interaction. Non-linear wave-wave interaction involves no loss of energy in itself because energy is simply "swapped" between different frequencies. However, the total amount of energy available for such "swapping" will gradually decrease, because higher frequency waves are more likely to dissipate energy. Wave attenuation is greatest in the generating area, where there are waves of many frequencies, and hence more opportunities for energy exchange between them. Waves drive net energy fluxes toward small scales, and the flux varies primarily with stratification, N^2, and internal wave energy density, E_{iw}, which is proportional to shear variance [Gregg (2021)]. As wave–wave interactions move energy to smaller scales, interactions become increasingly nonlinear until the waves break. Even though the breaking of internal waves happens at a much smaller scale (a few meters), and the generated dissipation, usually, at an even smaller scale (centimeters), it is of considerable importance for the vertical mixing in the ocean. In the simplest situation, turbulence develops from infinitesimal perturbations to steady laminar flow. However, in stratified profiles, the spatial scales of turbulence overlap those of internal waves. Therefore, in the open-ocean pycnocline, dissipation rates produced by breaking internal waves can be predicted from wave energetics [Gregg (2021)]. Munk and Wunsch (1998) estimated that of the 3.5 TW energy input from lunar and

solar tides, the background internal wave field only dissipates 0.2 TW. Distributing 0.2 TW of energy dissipated over the entire ocean volume $(1.33 \cdot 10^{18} \text{ m}^3)$ yields an average dissipation rate of $\varepsilon = 1.5 \cdot 10^{-10}$ W kg^{-1}. The background internal wave field, as mentioned in Section 2.2, mixes with an eddy diffusivity of $K_\rho \sim 10^{-5}$ m^2 s^{-1} [Gregg and Sanford (1988)].

2.4   Ozmidov Scale and Thorpe Scale

In the stratified interior, mixing occurs intermittently in turbulent patches. Density overturns contain microstructure patches, but microstructure patches can span multiple overturns [Gregg (2021)]. When calculating energy dissipation rates from turbulent patches, numerous problems and difficulties arise from sorting out similar events, leading Gargett and Garner (2008), and many others, to develop tests for validating overturns.

Two length scales are significant when using vertical overturns and temperature or density inversions to indirectly estimate the dissipation rate of turbulent kinetic energy in the ocean: the Ozmidov Scale (L_O) [Ozmidov (1965)] and the Thorpe Scale (L_T) [Thorpe (1977)].

The Ozmidov scale is given by:

$$L_O = \varepsilon^{1/2} N^{-3/2} \tag{4}$$

where ε is the dissipation rate of turbulent kinetic energy and N is the buoyancy frequency. L_O comes from a theoretical dimensional analysis: it is the maximum overturning length scale permitted in a stratified fluid. L_O is typically interpreted as the scale at which inertial forces balance buoyancy forces in the downscale cascade of turbulent kinetic energy [Gregg (1987)].

The Thorpe scale of an overturn is given by the root-mean-square of the vertical displacements (δ_T) of the water parcels in the depth range exhibiting the signature:

$$L_T = <(\delta_T)^2>^{1/2} \tag{5}$$

L_T is a direct physical measure of overturn size: it is a kinematic scale that describes the status of an overturn at the particular place and time of sampling [Mater et al. (2015)]. L_T reflects the available potential energy (ape), but is not strictly defined by it.

L_O and L_T are related energetically by the turbulent cascade process, but their correlation in ocean observations is fortuitous since L_O contains no direct information from overturns. Dillon (1982) provided observational evidence suggesting a linear relationship between them, that has then been supported by numerous studies (e.g. Ferron et al. (1998) and Stansfield et al. (2001)). Nevertheless, because of the spatial and temporal variability of the turbulent field and possible restratification effects, an exact linear relation is not to be expected. Instead, the relationship between L_O and L_T is a statistical one [Ferron et al. (1998)] and a large number of samples is required. If this statistical agreement is valid for a flow of interest, it allows for inference of the mean dissipation rate from a given set of conventionally measured density profiles, by using the equation:

$$\overline{\varepsilon_T} = a^2 \overline{L_T^2 N^3} \tag{6}$$

The overbar represents an ensemble average and a is the proportionality constant. Typically determined from an arithmetic mean (e.g. Dillon (1982)) or geometric mean (e.g. Ferron et al. (1998)) of L_O/L_T, a is generally suggested to be close to one.

The idea underlying Eq. 6 is quite simple, but the accuracy of the estimates of L_T is strongly dependent on all possible sources of error associated with data collection, processing, and interpretation [Gargett and Garner (2008)]. In particular, uncertainties in salinity calculations propagate into the calculated density, resulting in density profiles with higher noise levels than temperature profiles. However, temperature does not everywhere dominate the density gradient: in some oceanic regions, salinity contributes to and may even dominate seawater density. In that case, it is, hence, necessary to look for density inversions instead of temperature inversions.

Temperature and density profiles can be collected relatively easily and repeatedly by conductivity-temperature–depth profilers (CTD), and, therefore, Eq. 6 potentially represents a relatively accessible estimate of ε in comparison to direct measurements that require microstructure shear profilers [Mater et al. (2015)].

17

3   Methods

3.1   The Vertical Microstructure Profiler (VMP) and its Deployments during SONNET cruise

The Rockland Scientific International (RSI) Vertical Microstructure Profiler 250 (VMP-250-IR, SN417) is an internally recording, free-falling probe designed to measure velocity and temperature fluctuations in the water column. It can be used to evaluate micro-scale turbulence and estimate the dissipation rate of turbulent kinetic energy in the ocean. The instrument is shown in Fig. 6.

Figure 6: The Vertical Microstructure Profiler (VMP) secured on a deck of the Meteor Research Vessel. The temperature and shear probes are protected with white protection cases.

The VMP has a maximum depth rating of 1000 m. During the M180 SONNET expedition, it was equipped with a pressure sensor, two fast shear sensors oriented perpendicular to each other, a fast FP07 thermistor, and a slower recording compact CT (conductivity-temperature) sensor (see Fig. 7). The specifications of the sensors are summarized in Table 1. For deployments 3.3, 4.1, and 5.1 (the first number is the station number and the second one is the number of the block of casts at that station, so, for example, 4.1 corresponds to the first block of casts at station 4) the VMP was fitted with an additional FP07 temperature probe to rule out a potential damaging of the first thermistor. The manufacturer calibrated the shear sensors,

which contain a piezo-ceramic beam that measures fluctuations in the water flow. On the other hand, the thermistors and the pressure sensor required an in-situ calibration, that was carried out after the deployments.

Sensor	Parameter Measured	Range	Accuracy	Resolution	Band--width
PA-10L	pressure	0-10 bar	0.1% of FS	5×10^{-4} bar	0-2.5 Hz
Shear Probe	velocity shear	0-10 s^{-1}	5%	10^{-3} s^{-1}	0.1-100 Hz
FP07	temperature	-5-35 °C	0.005 °C	10^{-5}°C	0-25 Hz
CT	temperature	-3-45 °C	0.01 °C	0.001 °C	0-16 Hz
	conductivity	2-65 m S cm^{-1}	0.001 m S cm^{-1}	0.001 m S cm^{-1}	0-16 Hz

Table 1: Sensor specifications and instrument configuration for the VMP. FS is the full scale. Source: [Rockland (2021)]

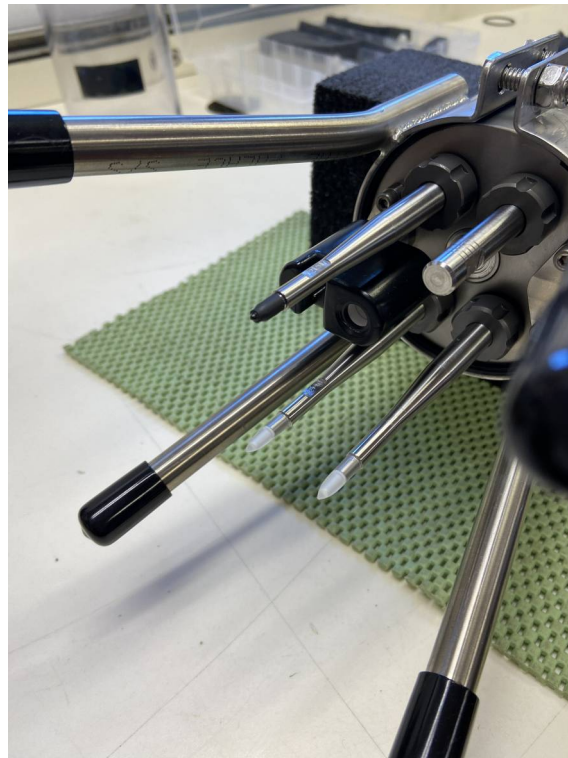Figure 7: Front bulkhead of the VMP with the sensors and sensor guard: pressure transducer (thin diaphragm located in the center of the front bulkhead), shear sensors (those with the white tip), FP07 thermistor (that with the black tip), and JAC, acronym for JFE Advantech Co., CT sensor (black small box between the FP07 thermistor and one of the shear sensors). The metallic cylinder next to the FP07 thermistor is a test probe.

The sensor guard, fixed to the front bulkhead and visible in Fig. 7, is designed to provide protection to the sensors without interfering with the measurements, and minimize vibrations from vortices shedding around the guard. The tail section of the VMP (see Fig. 6) helps stabilise the speed and vertical orientation of the instrument during profiling. During the deployments, both brushes were attached to the tail section, and, consequently, the average falling speed was about 0.6 - 0.7 m s^{-1}.

During the M180 SONNET expedition, a total of 21 blocks of microstructure measurements were performed, divided in eleven different stations, which can be seen in Fig. 4. The blocks of casts are listed in Table 2, and each of them contains three valid profiles, with deployment 5.2 being the only exception since it only has two valid profiles. With "valid" we mean that the VMP could fall freely and nonstop from the uppermost meters of the water column until a depth of at least 600m and that during the profile measure no complications with the winch or the rope occurred.

The VMP was deployed with a slowly (1 knot) drifting ship during the time series stations, mainly in between sets of Conductivity-Temperature-Depth (CTD) and Lowered Acoustic Doppler Current Profiler (LADCP) casts. A two-hour block of microstructure casts was sufficient to complete three profiles, with each profile taking about 40 minutes.

During a deployment, the VMP, secured by a rope, is lowered over the stern of the ship and falls freely to about 600 to 1000 m. Due to the fact that the rope in the water is inevitably tilted, it can be very difficult to estimate the actual depth at which the instrument is, even if the rope length is marked, especially during rough sea. Reached the desired depth, the instrument is recovered using a mechanical winch and directly re-deployed, since it is not necessary to bring the VMP back on deck between the profiles. The profiles can be separated later in data post-processing.

The deployments were usually done by a team of two people: one person operated the electric winch, while the other led the tether from the spool (in order to prevent the rope from getting stuck, knotted, or tangled) and checked that there was always enough rope in the water for the VMP to fall freely. Occasionally there were minor problems with the winch (mainly due to the rope jammed/stuck) which made it necessary to stop the deployments for a very short time during the downcasts. This rarely affected the falling speed of the instrument and its free fall, as usually there was enough slack in the water.

VMP Measurements List						
Station	**Block of Casts**	**Date**	**Time (UTC)**	**Latitude**	**Longitude**	**Regime**
3	1	2022.03.06	20:29	35°00'S	5°30'E	Eddy
3	2	2022.03.07	07:47	35°00'S	5°30'E	Eddy
3	3	2022.03.07	15:15	35°00'S	5°30'E	Eddy
4	1	2022.03.09	02:54	35°36'S	6°17'E	Eddy
5	1	2022.03.09	08:55	36°12'S	6°36'E	Eddy
5	2	2022.03.09	22:41	36°12'S	7°00'E	Eddy
5	3	2022.03.10	01:55	36°12'S	6°48'E	Eddy
5	4	2022.03.10	04:04	36°11'S	6°43'E	Eddy
14	1	2022.03.21	10:19	37°42'S	7°00'E	SMeso
15	1	2022.03.21	18:00	37°14'S	6°48'E	SMeso
16	1	2022.03.22	02:32	36°42'S	6°43'E	SMeso
20	1	2022.03.26	09:52	32°30'S	7°18'E	Beam
20	2	2022.03.26	19:33	32°30'S	7°18'E	Beam
21	2	2022.03.28	16:47	32°00'S	9°00'E	Beam
21	3	2022.03.29	00:55	32°00'S	8°60'E	Beam
22	1	2022.03.30	10:15	32°30'S	8°36'E	Beam
22	2	2022.03.31	03:56	32°30'S	8°36'E	Beam
23	1	2022.03.31	16:51	36°58'S	8°21'E	Beam
23	2	2022.04.01	08:47	32°58'S	8°21'E	Beam
28	1	2022.04.06	00:40	32°00'S	5°12'E	Beam
28	2	2022.04.06	12:05	32°00'S	5°12'E	Beam

Table 2: List of microstructure measurements (collected with the VMP during the SONNET expedition) with the respective station number, block number, date, starting time, latitude and longitude of the measurement site, and ocean regime of the corresponding area of study: Eddy for the Eddy Study Region, SMeso for the Submesoscale Study Region, and Beam for the Tidal Beam Study Region. During each block of casts, three valid profiles were measured, with deployment 5.2 being the only exception since it only contains two valid profiles.

3.2 The IfM14 Glider with Microrider (MR) and its Deployments during SONNET cruise

Gliders are versatile, autonomous, underwater vehicles that enable weeks of data collection for operations in coastal, offshore, under ice, and extreme conditions [Teledyne (2017)]. They can maintain stations or follow tracks against weak flows. Gliders can point microstructure probes into the flow while ascending and descending by moving the battery to shift the center of mass relative to the center of buoyancy [Gregg (2021)]. During the SONNET cruise, three different gliders were deployed, but only the data from one of them, namely IfM14, were analyzed for this Master's thesis. The IfM14 Glider is a Slocum G3 Glider. The deployment and recovery of a Slocum G3 Glider can take place from any size vessel and be operated by one or two people. Such gliders are buoyancy driven to enable long range and duration remote water column observation. Once the Slocum glider is deployed, it can easily be controlled from anywhere by using web based piloting tools. It can run pre-programmed routes, surfacing to transmit real time data to shore while downloading new instructions at regular intervals.

During SONNET, the IfM14 Glider was equipped with various sensors, including a CTD and internally recording MicroRider-1000 (MR) with 1000 m pressure rating. A MR is a modular, self-contained turbulence profiler for microstructure measurements. From the MR mounted on the glider, the dissipation of turbulent kinetic energy was obtained. The specifications of some of the sensors mounted on IfM14 are summarized in Table 3.

Sensor	Range	Accuracy	Resolution	Time Response
Velocity Shear	$3 \times 10^{-10} -$ -10^{-4} W kg^{-1}	5%	2.5×10^{-3} s^{-1}	
Water Temperature	-5-35 °C	1×10^{-3} °C	1×10^{-4} °C	0.070 s $\pm$ 0.010 s
Micro Temperature	-5-35 °C	N/A	1×10^{-5} °C	0.0.007 s $\pm$ 0.003 s
Conductivity	0-7 S m^{-1}	0.0003 S m^{-1}	0.00004 S m^{-1} at 24 Hz	0.060 seconds (pumped)
Pressure	0–1000 dbar	0.1 %	0.0005 dbar	
Micro Conductivity	0-7 S m^{-1}	N/A	~ 5 mm	infinite

Table 3: Sensor specifications of the MicroRider-1000. Source: Rockland Scientific.

3.3 Data Processing

3.3.1 VMP Data Correction

The VMP produces a raw data file according to user-supplied information in a configuration file (setup file) using the supplied data acquisition software. The RSI data acquisition software produces at least two files: a data file (a raw binary files with the extension ".p") and a log file that contains a record of the events that occurred during data acquisition. To process the collected data, RSI provides a Matlab Library (ODAS Matlab Library). The functions in the Matlab Library transform the raw binary file into a Matlab mat-file that can be used to convert the data into physical units and to conduct further processing of the data. Lueck et al. (2020) was used as a guide for the post-cruise data processing of the data files, and the technical details of each ODAS function are described in Douglas et al. (2020).

The acquired data needed some corrections before they could be studied. First of all, for each data file, the pressure calibration was performed. Within RSI instruments, changes in pressure are sensed as changes in voltage which is converted to units of decibars (dbar) in post processing. Due to constant changes in atmospheric pressure, the pressure sensors must be zeroed to sea level to accurately measure the water pressure. The "zeroing" of a pressure sensor is achieved by adjusting one coefficient (coef0) in the configuration file in post processing or immediately before a deployment.

A despiking of the shear, vibration, and micro-conductivity signals was performed. The conductivity signal was lagged and low-pass filtered to match the apparent response times of the conductivity and temperature signals, prior to computing the salinity.

Both raw signals and derived signals were converted into physical units, using information contained in the setup file, and the results were returned in a data structure.

The data measured by the FP07 thermistor were calibrated using in situ measurements from the JAC-CT over each profile in a file. To finalize this calibration, some of the determined coefficients (namely, T_0, beta_1, and beta_2) were averaged for the profiles of the block and input into the configuration string of the data file.

Finally, the data in the p-file were re-converted into physical units using the corrected setup file. A summary of processing parameters and data features for each VMP data file of the M180 SONNET expedition can be found in Table 10, Appendix A.

The single profiles corresponding to the successive casts during a deployment were separated and only the downcasts were considered. This is done in order to avoid, as much as possible, the interference in the water flow caused by the movement of the instrument.

In fact, the VMP is recovered using a mechanical winch and its path upward is therefore less smooth than its path when it is sinking freely.

The ODAS Matlab Library generates, for each profile of each data file, a Matlab output structure (called "diss") that contains the processed data: fields associated with the rate of dissipation of tke and shear spectra (for example ε), mean values at each dissipation estimate (for example speed, pressure, and temperature), fields associated with the despiking of the accelerometer, shear probe, and micro-conductivity signals, fields associated with the scalar signals, and additional parameters related to data processing. Each output structure depends slightly on the channels in the instrument. A relevant section of the structure is, obviously, the rate of dissipation of turbulent kinetic energy ε that is estimated from the velocity fluctuations in the water flow measured by the VMP, as

$$\varepsilon = \frac{15}{2}\nu\overline{\left(\frac{\partial u}{\partial z}\right)^2} \tag{7}$$

where $\frac{\partial u}{\partial z}$ is the shear and ν the kinematic molecular viscosity [Lueck (2016)]. In order to compute ε, the parameters in Table 4 were used.

Parameters	Values [s]
FFT length (FFT$_l$)	2
Dissipation length (D$_l$)	8
Overlap	4 (50%)

Table 4: Parameters used for calculating ε from the VMP data. These are all default processing parameters for the ODAS Matlab Library of Rockland Scientific, which are well suited to processing data collected with the VMP.

The lowest ε that a VMP can detect is in the 10^{-11} range, but it is possible that the instrument may only measure in the 10^{-10} range if there are many vibrations.

For each "diss" structure, the size of the matrix containing the rate of dissipation of turbulent kinetic energy is [N P], where N is the number of shear probes (2, during all deployments of SONNET), and P is the number of dissipation estimates (different for every profile).

One last correction was performed to the "diss" structures by calling an ODAS function which cleans, lags, and match-filters conductivity data from the JAC-CT sensor. This function reads the mat-file and uses it to generate a clean and corrected conductivity signal suitable for computing salinity by going through the following steps. First, it uses

the median filter to remove conductivity spikes. Then, it lags the conductivity signal by lag samples and low-pass filters the conductivity signal using a first-order Butterworth filter with a cut-off frequency to match this signal to the temperature signal. After that, it computes the salinity using the processed conductivity and the original temperature and pressure. Finally, the mat-file is updated with the corrected low-pass filtered conductivity signal, the salinity, and the indices of the data removed by the median filter.

3.3.2   VMP Data Analysis

In total, 62 "diss" structure files were obtained, one for each valid profile, i.e., considering all the measures, the deployment of 62 successful downcasts took place during the M180 SONNET expedition, as summarised in Table 5.

VMP deployments during SONETT	
Number of Stations	11
Number of Blocks	21
Number of Profiles	62

Table 5: Summary of valid VMP deployments during the SONNET expedition.

As mentioned in the previous section, the typical fields, among others, in the "diss" structure are associated with the rate of dissipation, with despiking, and with the scalar signals.

The further analyses of the collected data were performed using Matlab. A loop was used to import all "diss" files and save different variables in different matrices, with each column corresponding to a different downward profile. For each estimation of ε, two different values were measured since two shear probes were used during the deployments. We decided to use the arithmetic mean of the two estimates, except when they deviated by more than a factor of 2. In that case, only the lower estimation was kept.

Furthermore, we wanted to discard all ε estimates below 10^{-10} W kg^{-1}, to make sure that all our estimates were far above the sensitivity of the instrument. However, in the entire data set, there was no energy dissipation rate lower than 10^{-10} W kg^{-1}, probably due to some vibrations of the VMP during the deployments, meaning that it was not possible to measure and resolve dissipation at scales smaller than 10^{-10} W kg^{-1}.

All data corresponding to pressures that are less than 10 dbar need to be removed because they are likely to be affected by turbulence caused by the ship or by the VMP

itself entering the water. In this study, we want to focus the analysis on ocean layers that are deeper than the mixed layer. We are not interested in processes taking place close to the surface, but rather in turbulence caused by internal waves. Therefore, a starting pressure was sought by manually checking the vertical extent of the mixed layer in the temperature profiles for every deployment. A good common threshold value for pressure was found at 100 dbar. Starting the data analysis at this pressure, one can be sure that the water parcels in each profile are found in the ocean interior, below the mixed layer.

The main variables of interest in each "diss" structure are the energy dissipation rate ε, potential temperature, salinity, and density anomaly. These were used for the calculation of the diffusivity K_ρ of each profile, using Eq. 2, where Γ was set equal to 0.2 and N^2 was calculated with a function from the GSW Oceanographic Toolbox [McDougall and Barker (2011)].

Profile Averaging In order to have an overview of the dissipation at each location, mean profiles of every variable were calculated for each block and for each station. The averaging allows for more easily comparable vertical profiles since the data were collected at different rates for each downcast, due to the different falling velocities. Like the VMP vibrations, the instrument falling velocity is unfortunately very hard to control. In fact, it does not depend on the speed at which the winch is operated, as long as there is enough slack. Instead, the falling velocity is strongly influenced by the waves and sea conditions. As soon as the sea is slightly rough, the falling velocity starts oscillating a lot, as one can see in Fig. 8. Nevertheless, looking at the appearance of the dissipation profiles, it seems that such vibrations did not affect the measurements. In fact, in Fig. 8, no visible difference can be noticed between ε of profile 1 and ε of profile 3, even though the VMP falling velocity fluctuated much more in the first cast than in the third one. This is confirmed also by the comparison with other blocks of casts, during which the instrument fell very differently, even though it was deployed in the same way. For example, during all casts of block 4.1 (shown in Fig. 9) the falling velocity did not oscillate much, but steadily decreased from about 0.75 m s^{-1} in the mixed layer, to less than 0.65 m s^{-1} at the end of the profile. Dissipation profiles in Fig. 8 and Fig. 9 show similar behaviours, so we can conclude that velocity fluctuations did not significantly affect the measured dissipation in the detectable scales. Furthermore, no correlation was noted between the magnitude or trend of velocity fluctuations and time spent by the instrument (and rope) in the water.

Figure 8: Left: VMP falling speed as a function of pressure. Right: energy dissipation rate measured by the shear probes. These three profiles were collected during the first block of casts at station 23. Same colour corresponds to same profile in both plots. Nothing was changed in the way the instrument was deployed or operated during this block of casts. Nevertheless, the intensity and amplitude of fluctuations of the falling velocity decreased, especially in the deeper ocean, from profile 1 to profile 3.
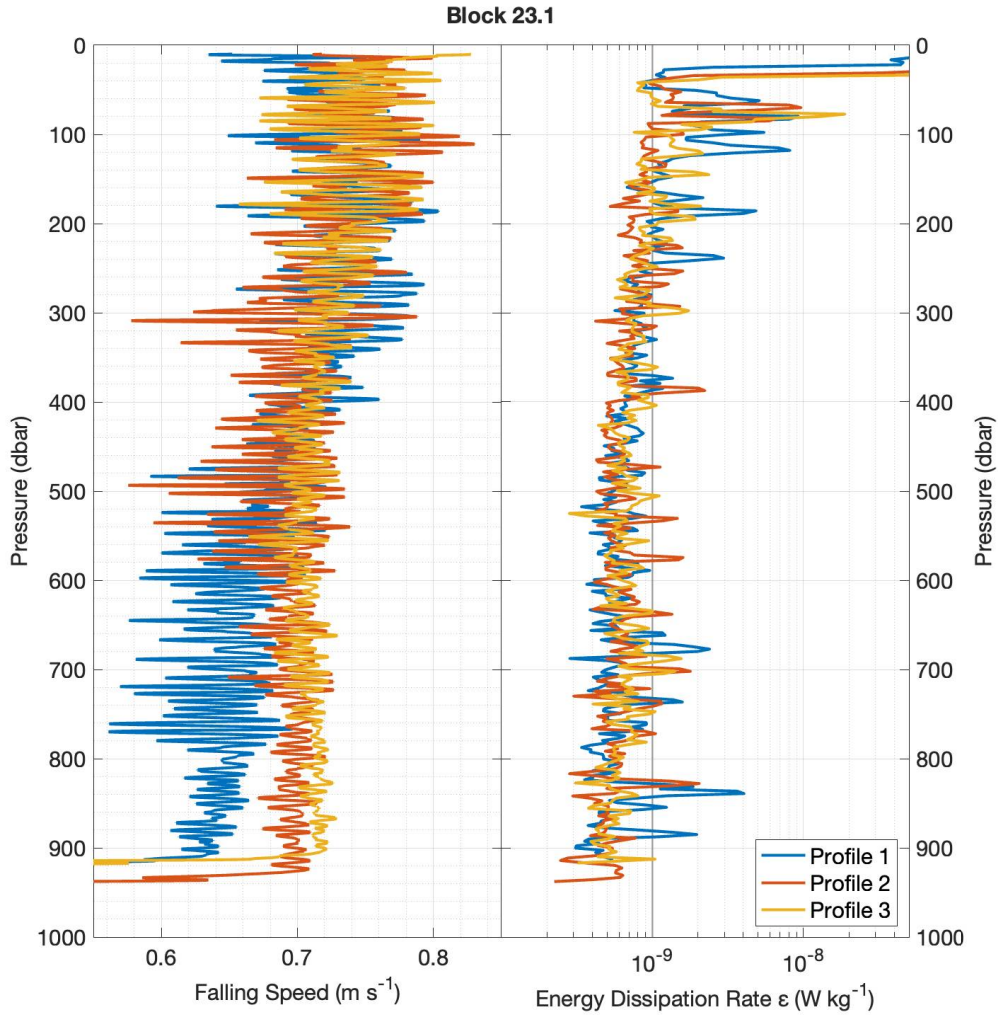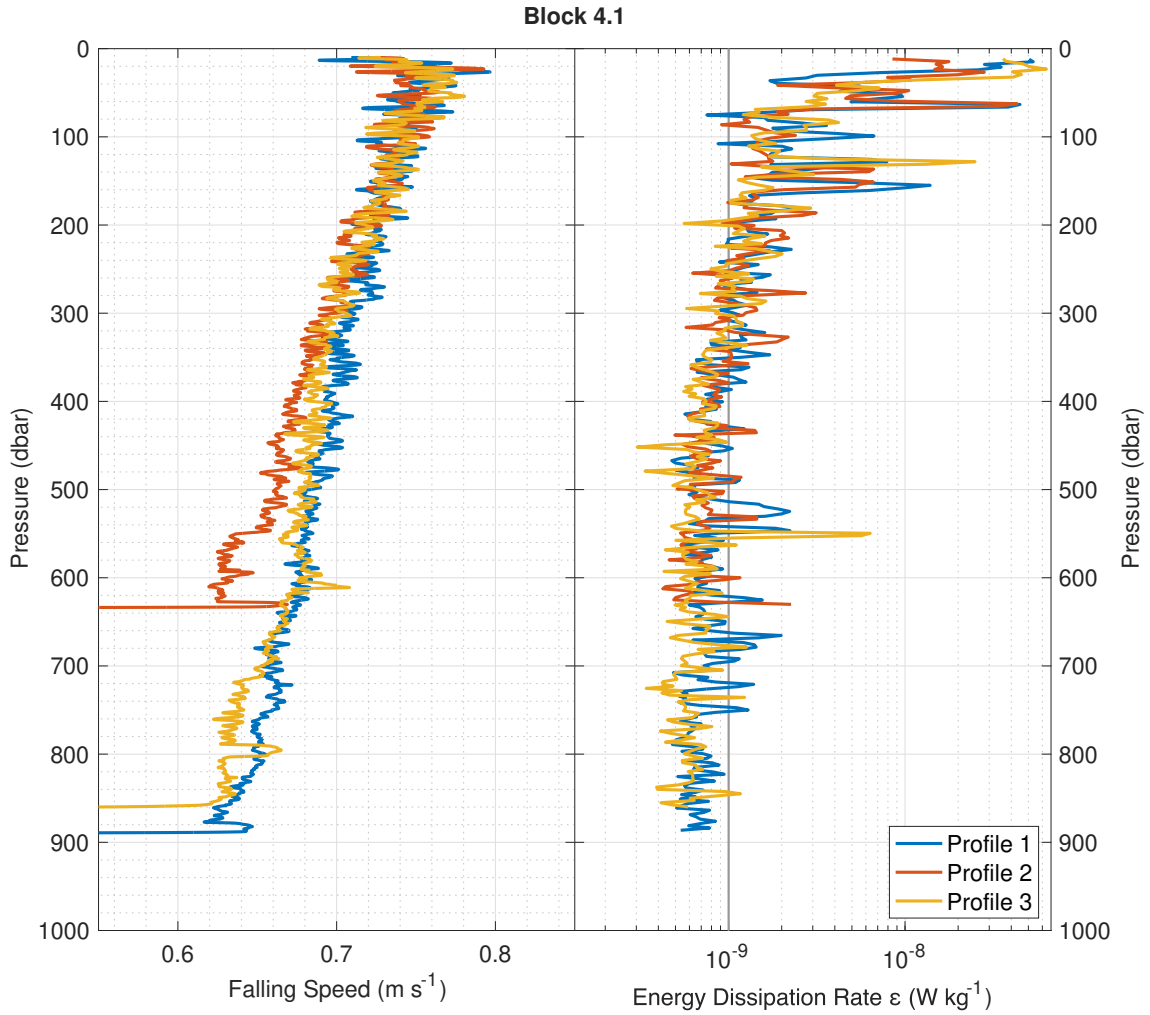
Figure 9: Left: VMP falling speed as a function of pressure. Right: energy dissipation rate measured by the shear probes. These three profiles were collected during the first block of casts at station 4. Same colour corresponds to same profile in both plots.

The mean profiles were calculated by first dividing the pressure profile in constant intervals of 5 dbar. Then, the mean value of a variable for a specific pressure interval is obtained by averaging all the data (for that variable) that correspond to the block or station under analysis and that fall inside the considered pressure range. The mean value is given by the average of typically 3 to 25 data, depending on the number of profiles that were averaged, on the falling speed, and on the depth. In fact, a different maximum pressure is reached in each profile, and, as already mentioned, the data were collected at a rate which was not constant due to the not constant VMP's falling velocity. When calculating the mean profile for a specific block or station if only one or two data were collected for a specific pressure interval, a NaN (not a number) is automatically assigned to that pressure interval. In fact, it is not meaningful to calculate the standard deviation

of only two numbers: they will necessarily be at the same distance from their mean value.

Three different estimates of the average value were calculated every time: the arithmetic mean, the geometric mean, and the median. The corresponding errors were also estimated using the standard deviation for the arithmetic mean, the geometric standard deviation for the geometric mean, and the standard error of the median for the median.

Depth Integrated Dissipation ϵ For each profile, the cumulative depth integrated energy dissipation rate was calculated by cumulatively integrating the ε profile over a part of the water column using the formula:

$$\epsilon = \rho \int_{z_s}^{z_f} \varepsilon dz \tag{8}$$

where ρ is density, z_s a starting depth, and z_f a final depth. The chosen starting depth was 100 m, that is slightly deeper than the layer of the pressure threshold (100 dbar), and the chosen ending depth was 600 m, since every profile reaches at least this depth. A cumulative trapezoidal numerical integration was performed for each epsilon profile and for the stations' means. To perform this calculation, the stations' mean profiles obtained by arithmetically averaging the profiles were used, as they are more sensitive to significant dissipative events.

For each valid profile and for each station, the final value (hence, corresponding to a depth of 600 m) of this cumulative integration is the depth integrated energy dissipation rate corresponding to that profile or station: ϵ. The error associated with ϵ is calculated as:

$$\delta\epsilon = \frac{\sigma(\varepsilon)}{\sqrt{N_\varepsilon}} \tag{9}$$

where $\sigma(\varepsilon)$ is the square root of the variance of the integrated dissipation profile and N_ε is the size of the integrated ε sample. Table 7 lists ϵ estimates for all 11 stations, the same results are also plotted on a map in Fig. 25.

Using the cumulative integrals of the single ε profiles, we wanted to estimate the contribution of both outstanding and smallest turbulent events to the total depth integrated dissipation of that profile. To do so, for each ε profile, a smoothed dissipation curve was calculated and plotted. Such curve follows the trend with depth of the ε profile without showing the peaks caused by individual dissipative events. We defined it as the background energy dissipation, yet such dissipation is also caused by turbulent events, but these are too small to be resolved by the VMP. For each profile, the (or one of the) most outstanding turbulent event between 100 and 300 m and the (or one of the) most outstanding turbulent event between 300 and 600 m were manually identified. Fig. 10 shows

the measured ε profile, the calculated background profile, and the two selected dissipative events for profile 3, fourth block of casts, station 5.
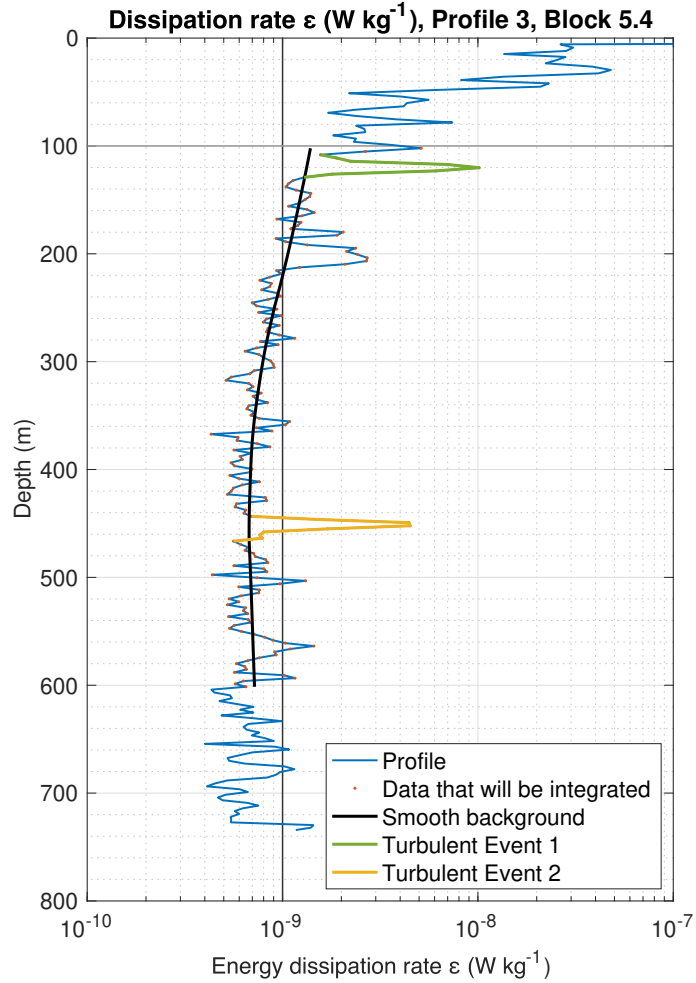
Figure 10: Energy dissipation rate for profile 3, block of casts 4, station 5 as a function of depth. The black curve is a smoothed version of the profile and corresponds to the dissipation background between 100 and 600 m. The orange dots are the data points. Two dissipative events, that will be integrated separately, are underlined. The green one (turbulent event 1) is in the upper part of the dissipation profile, while the yellow one (turbulent event 2) is in the lower part of the profile. The horizontal dark gray line indicates the horizon corresponding to a pressure of 100 dbar. The vertical dark gray line corresponds to 10^{-9} W kg^{-1}: a good approximation for the order of magnitude of the energy dissipation rate.

Three more integrations with depth were performed for every profile: one for the smooth background curve and one for each of the two individual selected spikes. The ratios of each of these integrals and ϵ give the percentage contributions to ϵ of the background mixing and of the selected dissipative events, respectively. Finally, the percentages

resulting from all the different profiles were averaged, and the standard deviation of each contribution was calculated. Table 11 in Appendix B lists the results of such integrations and ratios.

Evaluation of the amount of total dissipated energy The total amount of energy dissipated by internal waves in the studied area was computed. To do so, a mean constant density ($\overline{\sigma} = 1027$ kg m^{-3}) was multiplied by a mean energy dissipation rate ($\overline{\varepsilon} = 0.9 \cdot 10^{-9}$ W kg^{-1}) and by the volume of the considered study area ($V_{study} = 1.06 \cdot 10^{14}$ m^3). The mean density and the mean energy dissipation rate were obtained by arithmetically averaging all the data collected with the VMP in the ocean layer between 100 and 600 m, during the SONETT cruise. The volume of the study area, V$_{study}$, was calculated as:

$$V_{study} = D \cdot \delta(\phi) \cdot \delta(\lambda) \cdot \frac{cos(\lambda_{min}) + cos(\lambda_{max})}{2} \cdot (111 \text{ km})^2$$

where D = 0.5 km is the depth of the water layer between 100 and 600 m, $\delta(\phi)$ and $\delta(\lambda)$ are the differences between the minimum and the maximum latitude and longitude, respectively, at which the VMP was deployed, and λ_{min} and λ_{max} are the minimum and the maximum longitude at which the VMP was deployed. Their cosine and the factor 111 km are used when converting the degree of latitude and longitude into kilometers. The result obtained is $V_{study} = 1.06 \cdot 10^5$ km$^3 = 1.16 \cdot 10^{14}$ m^3.

Calculation of energy dissipation rates from Thorpe Scale In order to calculate the Thorpe Scale, the temperature and conductivity profiles measured by the JAC CT and the corresponding high-resolution pressure profiles are loaded into Matlab workspace. The different variables are saved in different matrices, with each column corresponding to a different downward profile. All data corresponding to a pressure that is less than 10 dbar are discarded, but also the data between 10 and 100 dbar are not considered in the further analysis, as the study of the mixed layer is not the subject of this thesis. Potential temperature, depth (meaning distance from the sea surface), conservative temperature, and density were calculated for each profile using the Gibbs SeaWater (GSW) Oceanographic Toolbox of TEOS-10 [McDougall and Barker (2011)].

The following step was to calculate the Thorpe scale L_T. Thorpe (1977) proposed to sort monotonically and adiabatically the vertical profile of temperature containing small temperature inversions to obtain a stable temperature profile. The difference $d = z_0 - z_r$ between the original (z_0) and ordered (z_r) positions of each fluid parcel in the temperature profile, if $d \neq 0$, can be interpreted as an estimate of the vertical displacement d asso-

ciated with turbulent motions. Positive displacements d correspond to upward motion, while negative d to downward motion. These nonzero displacements take place where instabilities, i.e. temperature inversions, exist in the measured profile. In fact, temperature and salinity fluctuations determine the density stratification suppressing turbulence. Where salinity gradients are weak, for example in Loch Ness, where Thorpe (1977) carried his study, energy-containing scales can be easily resolved with temperature. Elsewhere, where the salinity gradient is important, such as near the Walvis Ridge, salinity must be inferred. Nevertheless, mismatches in resolution between simultaneous measurements of temperature and conductivity probes can generate salinity spikes that obscure the stratification. When processing the data after the cruise, the salinity spikes were removed, and we decided to use density inversions instead of temperature inversions. In fact, the measured temperature profiles often showed inversions that were salinity compensated: in correspondence to such temperature inversions, there were no inversions in the density profile.

Then, as showed by Eq. 5, the Thorpe scale can be calculated as the root-mean-square (rms) value of the displacements for each turbulent patch, that is a vertical segment of the profile over which nonzero values of d cumulatively sum to zero [Mater et al. (2015)]. Therefore, to each unstable structure, a typical displacement (L_T) is assigned, which is characteristic of the overturn vertical length scale. The minimum resolvable Thorpe scale depends on the sampling rate and the noise level of the instrument [Ferron et al. (1998)].

The algorithm used for the search of density inversions and the validation of overturns is based on the steps proposed and reported by Ferron et al. (1998) with the addition of the corrections described by Gargett and Garner (2008). The method from Ferron et al. (1998) takes into account the instrumental noise that contaminates the measurements. Such consideration is of particular relevance when stratification is weak. In fact, the computation accuracy of the displacements d depends on both the instrument noise level and the local mean vertical gradient of measured temperature (density). An inversion may appear due to noise if the temperature (density) gradient is sufficiently low. Therefore, ordering the raw profile makes it impossible to distinguish between noise inversions and real inversions. In order to limit such error, Thorpe (1977) suggested to set d to zero whenever the temperature (density) in the measured profile differs from the temperature (density) of the ordered profile taken at the same pressure level by less than the instrument noise. Nevertheless, Thorpe's method tends to underestimate the length of the overturn by rejecting valid displacements located in the weakest temperature (density) gradient. To

avoid that, Ferron et al. (1998) described how to process the raw measured profile in order to obtain and use an intermediate temperature (density) profile which is only composed of fluctuations that are relevant to the accuracy of the measurement. The determination of the accuracy value is based on the magnitude of random noise levels in sea-water temperature (density). Because in situ noise levels may exceed manufacturer statements for a variety of reasons, noise is determined using actual cruise profiles, following Gargett and Garner (2008). Some well mixed layers (and their starting pressure) are manually identified and chosen simply by looking at the plotted density profiles. The property noise level is the result of the standard deviation of density values within these in-density-well-mixed layers. Different threshold values result from different choices of "well mixed" layers within the cruise data set. The chosen layers and the resulting noise are listed in Table 12 in Appendix C. The noise mean over all layers ($0.0027 \, \mathrm{kg} \, \mathrm{m}^{-3}$) was used as accuracy value, i.e. threshold level for identifying density inversions in the density profiles. Moreover, the intermediate profile is influenced by the starting value, hence two intermediate profiles were calculated for each density profile: one from the top to the bottom and one from the bottom to the top. The average of these two intermediate profiles was used as actual intermediate profile because it follows the actual profile more closely than either of the individual intermediate profiles. As an example, an enlargement of the density profile and of its corresponding various intermediate profiles, from the second profile of the second block of casts at station 3, is shown in Fig. 11.

Then, the intermediate profile is sorted and the vertical displacements d were calculated by comparing the mean intermediate profile and the sorted intermediate profile. Fig. 12 shows an enlargement of the mean intermediate density profile and of the sorted mean intermediate density profile for profile 2, block of casts 2, station 3, between 314 and 319 dbar. Also the water parcels displacements corresponding to that depth interval are illustrated.

After calculating the vertical displacements, the following step was to locate the turbulent patches within the profiles. As previously mentioned, a turbulent patch is a region within which the displacements sum up to zero:

$$\sum d = 0$$

Therefore, the zeros given by a cumulative sum of the displacements of each profile were used in order to identify the beginning and the ending of each turbulent patch. Summation was always started at the bottom of the profile and proceeded upward to avoid induced problems with near-surface data.
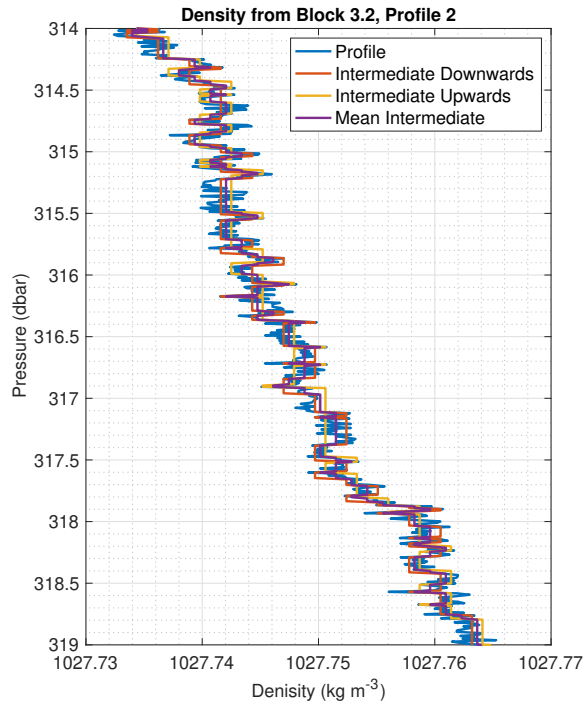
Figure 11: Enlargement (between 314 and 319 dbar) of the measured density profile (blue), upward intermediate density profile (orange), downward intermediate density profile (yellow), and mean intermediate density profile (purple) for profile 2, block of casts 2, station 3.
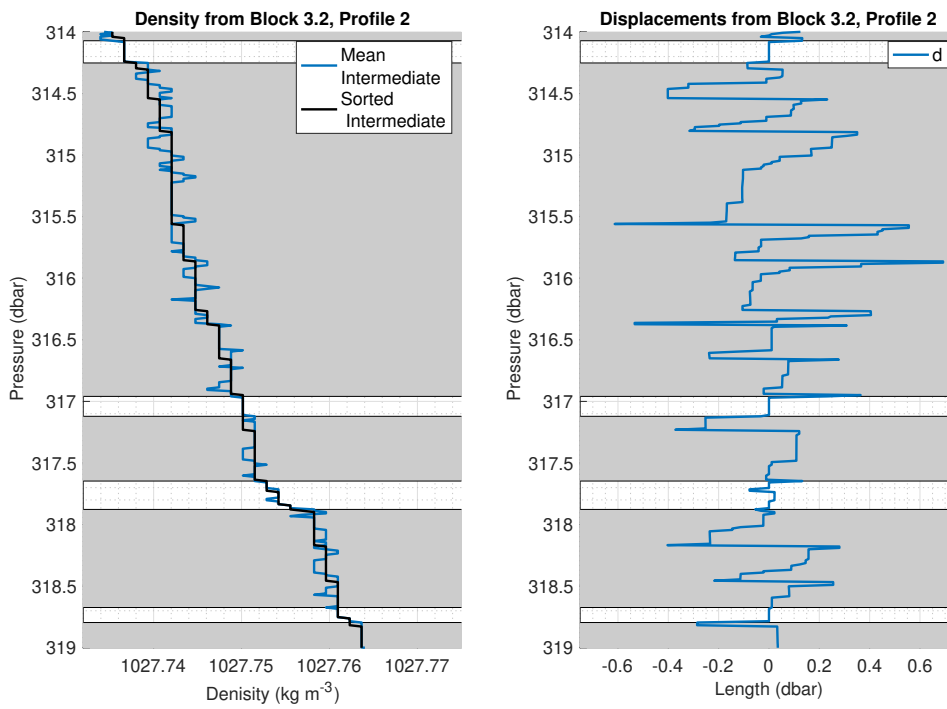
Figure 12: Enlargement between 314 and 319 dbar for profile 2, block of casts 2, station 3. Left: mean intermediate density profile and sorted mean intermediate density profile. Right: Displacements d of the water parcels. The areas with a gray background underline a turbulent patch.

Moreover, Gargett and Garner (2008) developed a method for the identification of suspect overturns based on diagnostics calculated after the individuation of overturning regions. The overturning ratio R_o is defined as:

$$R_o = min(L^+/L, L^-/L)$$

where L^+ and L^- are, respectively, the vertical distances occupied by positive and negative displacements within an overturn of vertical extent L. A single perfect overturn sampled would contain equal lengths of positive and negative displacements ($R_o = 0.5$), while a more complex and/or imperfectly sampled overturn would have $R_o < 0.5$. See Gargett and Garner (2008) for more details and some examples. Inspecting a large number of profiles, Gargett and Garner (2008) found that density overturns that would be declared suspect as a result of residual salinity spiking in an otherwise weakly stratified region are associated with values of $R_o < 0.2$. In such cases, in fact, there is a small number of large displacements in one direction (either positive or negative), corresponding to the points within the spike, accompanied by a large number of small displacements in the other direction, as all the remaining points shift slightly to accommodate the point inside the spike. Such situations are characterized by low values of the overturning ratio. Therefore, all overturns with $R_o < 0.2$ were disregarded.

For the calculation of L_T, only turbulent patches with at least six samples were considered (roughly, patches larger than 0.1 dbar), as suggested by Smith (2019). In fact, 2925 of 50222 total patches have five or fewer samples. Most of these apparent patches are very small: 479 are the minimum two-point reversals, and more than one-third contain a maximum of three points. It seems reasonable to ignore these patches as probably being at least partially a product of the noise level of the sensors and, in any case, not significant in terms of either turbulent dissipation or mixing of density.

Then, for each turbulent patch, the Thorpe Scale L_T was computed using Eq. 5 and then converted from dbar to metre. In Fig. 13, L_T (in dbars and in meters) of each turbulent patch between 314 and 319 dbar is shown for profile 2 of block 2 at station 3.

To calculate the dissipation rate ε_T, also the buoyancy frequency $N = \sqrt{\frac{-g}{\rho_0}\frac{\partial \rho}{\partial z}}$ is needed, where g is the gravitational acceleration, ρ_0 is the density of the parcel of water, and $\frac{\partial \rho}{\partial z}$ is the density gradient. The mean intermediate sorted profile was used as surrogate for the background stratification profile against which a particular overturn is working. The gradient of the profile across a turbulent patch was calculated by taking the values of absolute salinity, conservative temperature, and pressure at the depth just before the starting of the turbulent patch and at the depth just after its ending.

Figure 13: Left: Thorpe Scale of the turbulent patches between 314 and 319 dbar as a function of pressure for profile 2, block of casts 2, station 3. Right: same plot, but dbars (unit of pressure and length) have been converted into metres (unit of depth and length).

The value of N^2 for each overturn region was obtained with a function from the GSW Oceanographic Toolbox [McDougall and Barker (2011)]. Now that a Thorpe scale L_T and a buoyancy frequency N are associated to each specific turbulent patch, Eq. 6 can be used for determining the corresponding ε_T by assuming $a = 1$. Fig. 14 shows an enlargement of profile 2, block of casts 2, station 3: N^2 (on the left) and ε_T (on the right) of each turbulent patch between 314 and 319 dbar.

I was, then, interested in comparing the ε_T profiles with the ε profiles obtained from the velocity fluctuations measured by the shear probes. The estimates of ε_T are piecewise constant, therefore, in order to be consistent with these, for each profile, ε estimations were interpolated in the middle of each turbulent patch found in the simultaneously collected density profile. Such value (the interpolation of ε in the middle of the turbulent patch) was assigned to the entire vertical interval that coincides with the considered turbulent patch. In this way, a new piecewise constant dissipation, denoted as ε_O, was obtained for each profile.
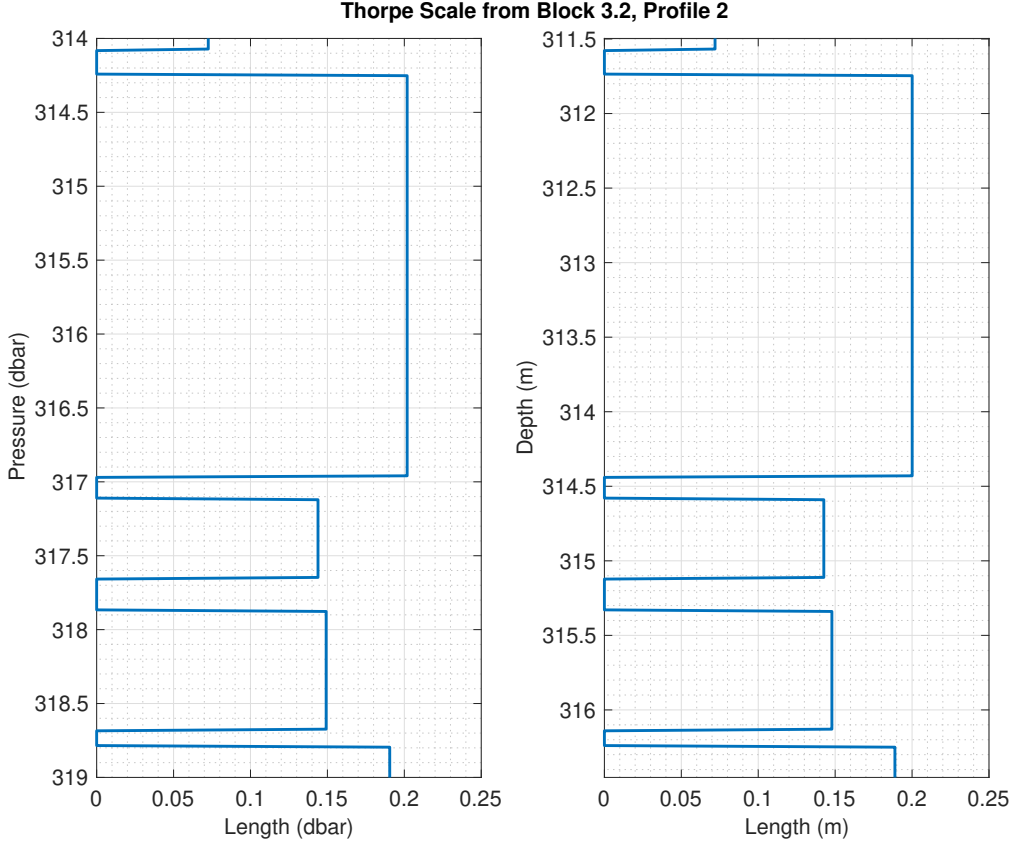
36

Figure 14: Left: buoyancy frequency N^2 of the turbulent patches between 314 and 319 dbar as a function of pressure for profile 2, block of casts 2, station 3. Right: energy dissipation rate ε of the turbulent patches between 314 and 319 dbar as a function of pressure for the same profile.

Using again a part of profile 2, block of casts 2, station 3 as an example, Fig. 15 shows the dissipation directly estimated from velocity fluctuations (ε), the new piecewise constant profile (ε_O), and the dissipation obtained from density inversions (ε_T).

For each turbulent patch, the Ozmidov Scale was also calculated by inserting ε_O into Eq. 4 (see Fig. 16). Now it is finally possible to compare L_T and L_O, to study their relationship and compute an estimation for the proportionality constant a between the two scales.
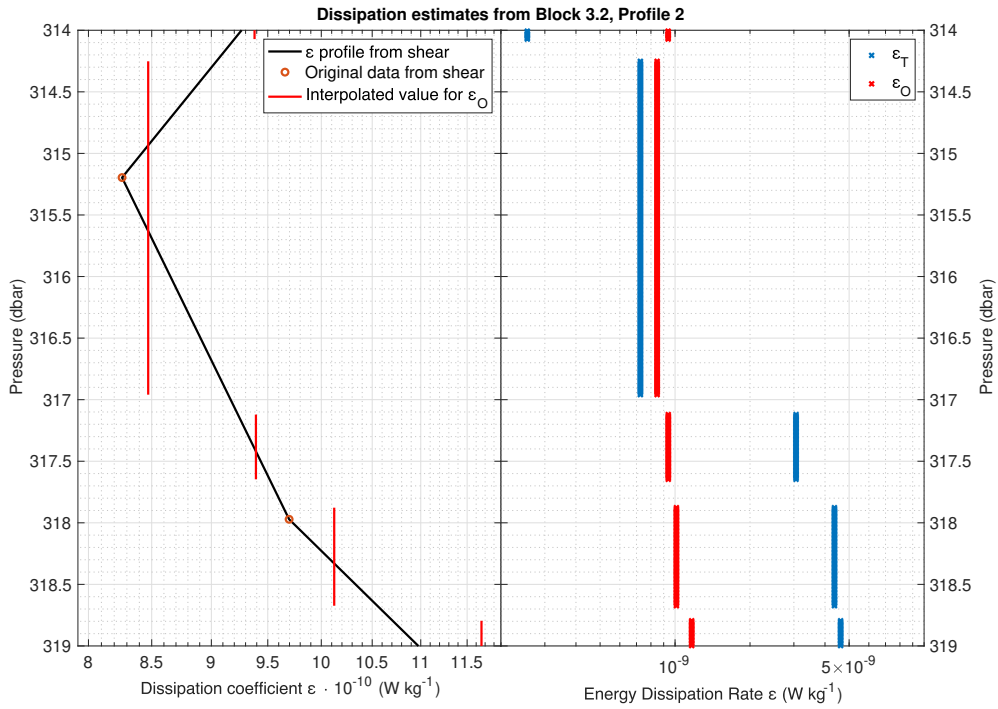
Figure 15: Enlargement for profile 2 of block 3.2, between 314 and 319 dbar. Left: directly estimated dissipation ε (orange data connected by the black line) and new piecewise constant ε_O (red lines), obtained by assigning to the pressure interval corresponding to a turbulent patch a dissipation value calculated by interpolating ε in the middle of the turbulent patch. Right: piecewise constant dissipation from velocity fluctuations (ε_O, red) and dissipation estimates from L_T (ε_T, blue). Note that while ordinates of the two plots are the same, the abscissa scale changes.
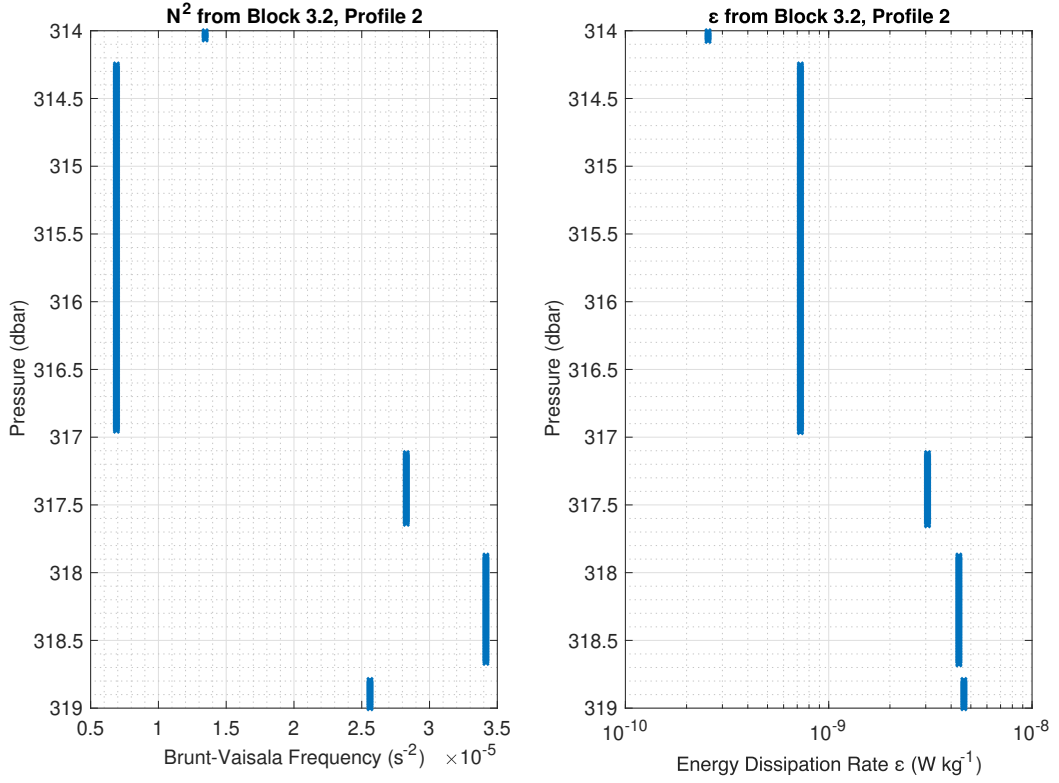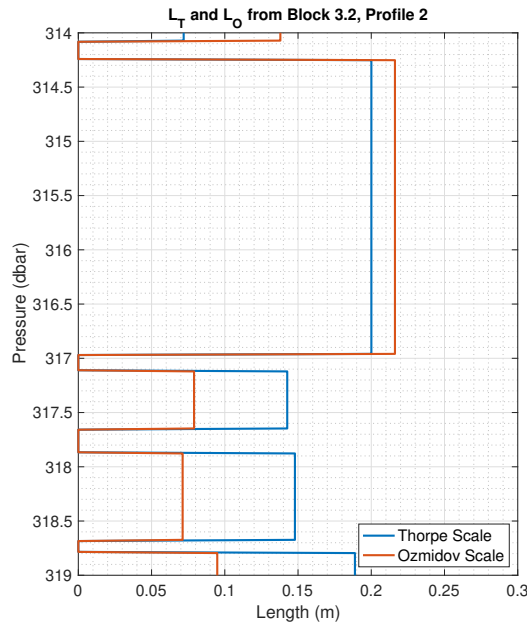

Figure 16: Thorpe Scale (blue) and Ozmidov Scale (orange) of the turbulent patches between 314 and 319 dbar as a function of pressure, for profile 2, block of casts 2, station 3.

A direct comparison of the Thorpe and the Ozmidov Scales for all turbulent patches is obtained with a scatter plot of $log(L_T)$ vs $log(L_O)$, and the distribution of L_T/L_O is studied with a histogram of all the values of $log(L_T/L_O)$ and by fitting a normal density function, see Fig. 28. The number of bins was chosen in order for every bar to cover an interval of length 0.01. The mean value of the L_O/L_T ratio and its standard deviation give the value of the proportionality constant a and of its error, respectively. This estimation for a will be denoted as a' and used for a new calculation of ε_T profiles (indicated by ε'_T), through Eq. 6. Finally, both the dissipation rates ε'_T and ε, i.e. the one directly measured, were averaged as a function of density, allowing for a comparison between the mean profiles ($\overline{\varepsilon'_T}$ and $\bar{\varepsilon}$) obtained with the two methods. For each station, the averaging was performed over all the profiles of that station by considering two density values as the same one if their difference is within a certain tolerance. The chosen tolerance is 0.027 kg m^{-3}, exactly ten times bigger than the accuracy value used when calculating the intermediate density profiles. This density averaging method was applied in order to reduce the effect produced by vertical advection downstream of a sill or by internal waves. In fact, single turbulent patches may move vertically and be found at different pressures or depths in different profiles, but their density is unlikely to change. This vertical movement would spread and lower the intensity of Thorpe scales if depth or pressure averaging was used. The $\overline{\varepsilon'_T}$ and $\bar{\varepsilon}$ profiles are shown in Fig. 29.

3.3.3 Processing of MR Data

The processing of glider and MR's data was carried out by Mariana Miracca Lage, from the Helmholtz-Zentrum hereon, and will be summarised here. First, it was necessary to match each MR file with the corresponding glider file with respect to time. Then, the MR files were converted into physical units using ODAS MATLAB toolbox (Version 3.1.1) and a proper configuration file (that contains the information about which sensors were used in which glider/MR). Also, time and pressure shifts between files were corrected, and glider variables were interpolated into the MR's grid. In order to compute ε, different functions from ODAS and the parameters in Table 6 were used.

The data were, then, despiked using thresh $= 7$, smooth $= 0.5$, and N $= 0.03 \cdot$ frequency (spike removal scale) ~ 15. Thresh is the threshold value for the ratio of the instantaneous rectified signal to its smoothed version, while smooth is the cut-off frequency of the first-order butter filter that is used to smooth the rectified input signal. Finally, a 4th order high pass butter filter with a window of $1/\mathrm{FFT}_l$ was applied and the dissipation was calculated

if the length of the shear vector was larger than D_l. In order to test the first estimates of ε, some quality controls were performed, including testing on Taylor's hypothesis of frozen turbulence, applying the Goodman algorithm, and calculating the Index of Spectral Agreement (ISA) as in Schultze et al. (2017). Consequently, the ε estimates from both sensors were compared: if they differ by more than a factor of four but their ISA are within a 10% range, the minimum value was chosen, if the estimates differ by more than a factor of four and ISA differs by more than 10%, the value with the spectrum with the higher quality was chosen. In all other cases, the arithmetic mean between estimates of the two probes was taken.

Parameters	Values [s]
FFT length (FFT$_l$)	4
Dissipation length (D$_l$)	12
Overlap	6 (50%)

Table 6: Parameters used for calculating ε from the MR's data

3.3.4   Analysis of MR Data

The further analysis of the data collected with the IfM14 glider was performed using Matlab. The glider data were interpolated using MR data so that, for each ε estimate, one has the corresponding depth, time, and geographical coordinates (longitude and latitude), as well. A loop was used in order to identify dives and climbs of the instruments and create a matrix for each variable containing a different profile (either downward or upward) in each column. With the IfM14 glider, 129 different valid profiles were collected. Only data corresponding to a pressure that is higher than 100 dbar were taken into account.

Depth Integrated Dissipation ϵ For each profile, the depth integrated energy dissipation rate (ϵ) was calculated between 100 and 600 m, by integrating the ε profile following Eq. 8. The general approach was the same as the one used for calculating ϵ for the VMP data. The resulting ϵ, one for each profile measured by the MR, are shown on a map in Fig. 30, and listed in Table 13 in Appendix D.

When consistently comparing the MR data with the VMP data, all ε estimates from the MR that were lower than 10^{-10} are discarded before calculating ϵ again. In fact, the MR has a lower noise level that the VMP, allowing for the measurement of much smaller ε.

40

Moreover, I grouped the MR profiles inside six non-equisized subareas and arithmetically averaged the depth integrated dissipation ϵ of the profiles inside each area. Information about these subareas and their mean ϵ (denoted as $\bar{\epsilon}$) can be found in Table 8. Such results ($\bar{\epsilon}$) were plotted on a map (Fig. 31) together with the depth integrated energy dissipation rate for each VMP station.

Similarly to what was done with the profiles collected with the VMP, the contribution of the smallest detectable mixing to the total depth integrated dissipation (ϵ) of each profile was calculated. Fig. 17 shows the measured ε and the computed "background" for one MR profile (profile 45). Then, the mean, over all 129 profiles, of the ratio between the integral of the smoothed dissipation curve and the integral of the measured profile was calculated.
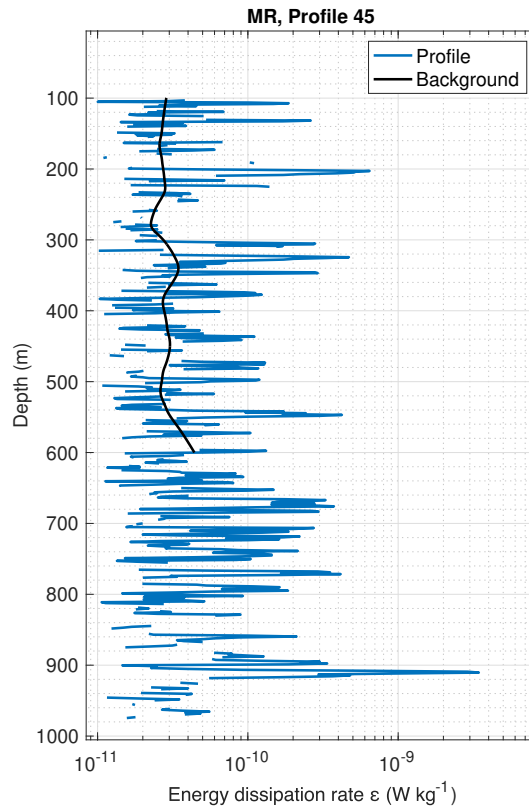
Figure 17: Energy dissipation rate profile for profile 45 as a function of depth. The black curve is the "background" smoothed version of the profile between 100 and 600 m.

41

4 Results

4.1 VMP

For each profile, the "diss" structure contains some important properties of sea water that were directly measured during the deployments of the VMP. Fig. 18, 19, and 20 show some examples. For all the profiles of blocks 3.2, 5.4, and 23.1, respectively, the energy dissipation rate ε, potential temperature, and salinity are plotted, one next to the other. Also the calculated diffusivity, K_ρ, and buoyancy frequency, N^2, are shown. Some blocks do not show particularly interesting features: all the profiles are very similar and without remarkable sudden variations in the temperature and salinity profiles (for instance 3.2, Fig. 18).

Figure 18: Energy dissipation rate, diffusivity, buoyancy frequency, potential temperature, and salinity for the three profiles measured during the second block of casts at station 3. Same colour corresponds to same profile in all plots. The horizontal gray line indicates the horizon corresponding to a pressure of 100 dbar. The vertical gray lines correspond to $\varepsilon = 10^{-9}$ W kg^{-1}, $K_\rho = 10^{-5}$ m^2 s^{-1}, and $N^2 = 10^{-5}$ s^{-2} in the first, second, and third plots from the left, respectively.

On the other hand, temperature and/or salinity profiles of other blocks, such as 5.4

(Fig. 19), feature notable and rapid changes that sometimes disappear when looking at the density profiles. Moreover, in some blocks, it is possible to notice oscillations that may well be the effect of internal waves. For example, in block 5.4, between about 50 and 100 m, the potential temperature in profile three appears "lifted", compared to profile two and four. In block 23.1 (Fig. 20) one can observe, in the temperature and salinity profiles, how the depth of the mixed layer increases among the profiles (i.e. with time), and becomes sharper due to turbulence occurring in the mixed layer. Note that profiles are collected about 40 minutes apart. As for ε, some profiles contain more fluctuations (e.g. in block 23.1) while other feature peaks that extend for a greater depth (e.g. in block 5.4), but all tend to show the same trend: the rate of energy dissipation decreases slightly with pressure. It is often of the order of 10^{-9} from the bottom of the mixed layer up to about 300 dbar while deeper down it tends to be less than 10^{-9}, except for some peaks, that correspond to dissipative, turbulent events.
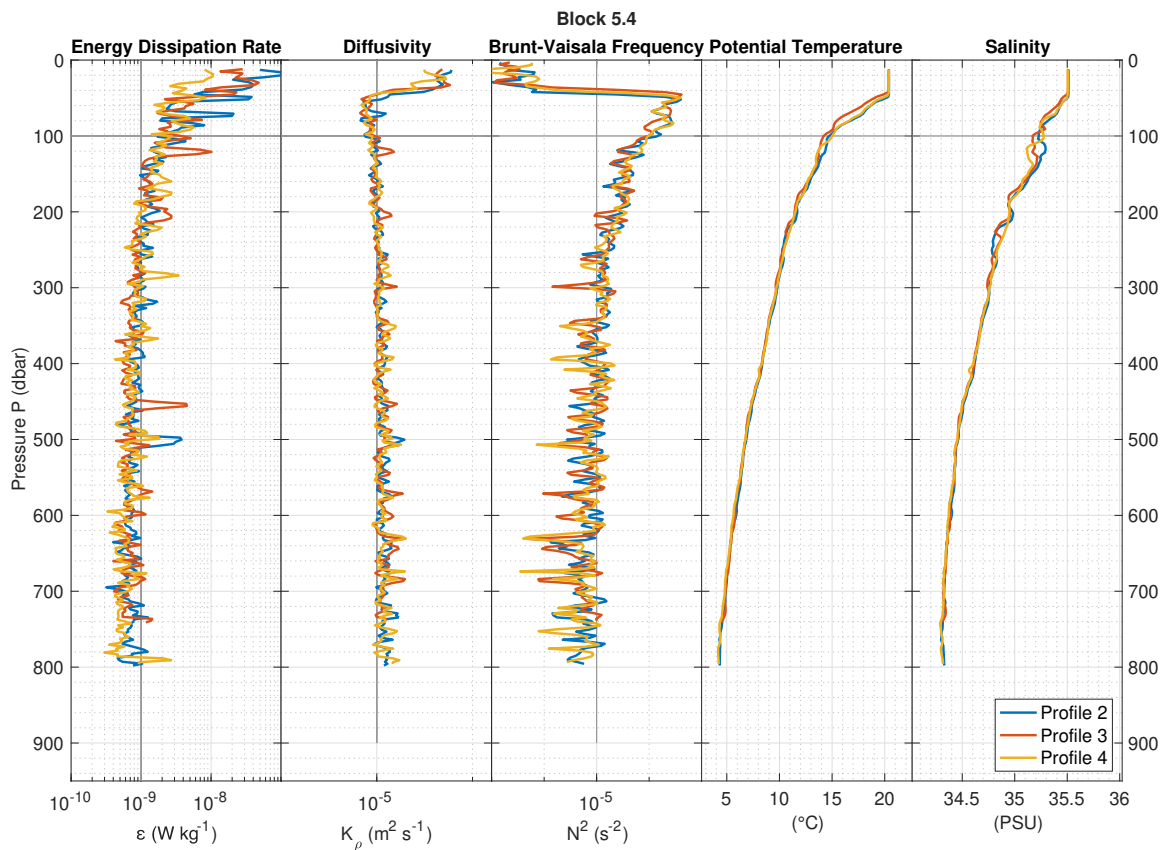
Figure 19: Energy dissipation rate, diffusivity, buoyancy frequency, potential temperature, and salinity for the three profiles measured during the fourth block of casts at station 5. Same colour corresponds to same profile in all plots. The horizontal gray line indicates the horizon corresponding to a pressure of 100 dbar. The vertical gray lines correspond to $\varepsilon = 10^{-9}$ W kg^{-1}, $K_\rho = 10^{-5}$ m^2 s^{-1}, and $N^2 = 10^{-5}$ s^{-2} in the first, second, and third plots from the left, respectively.
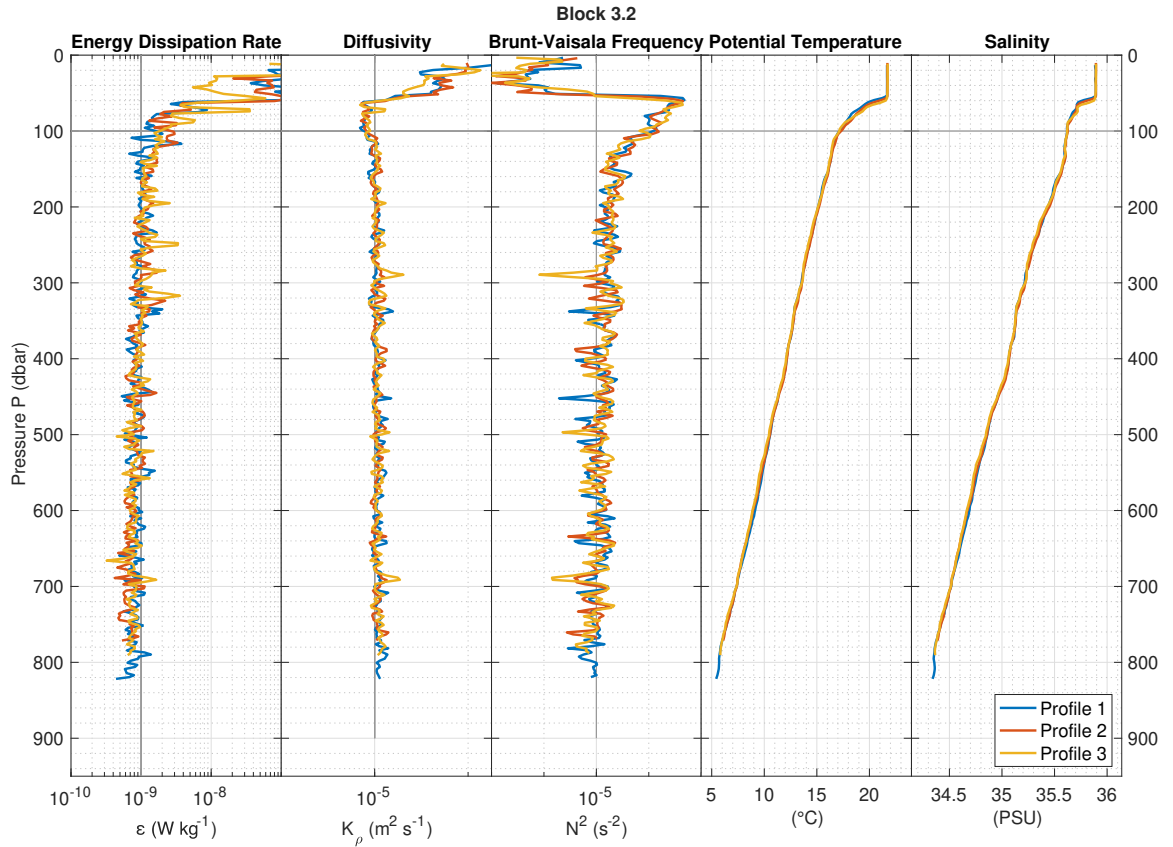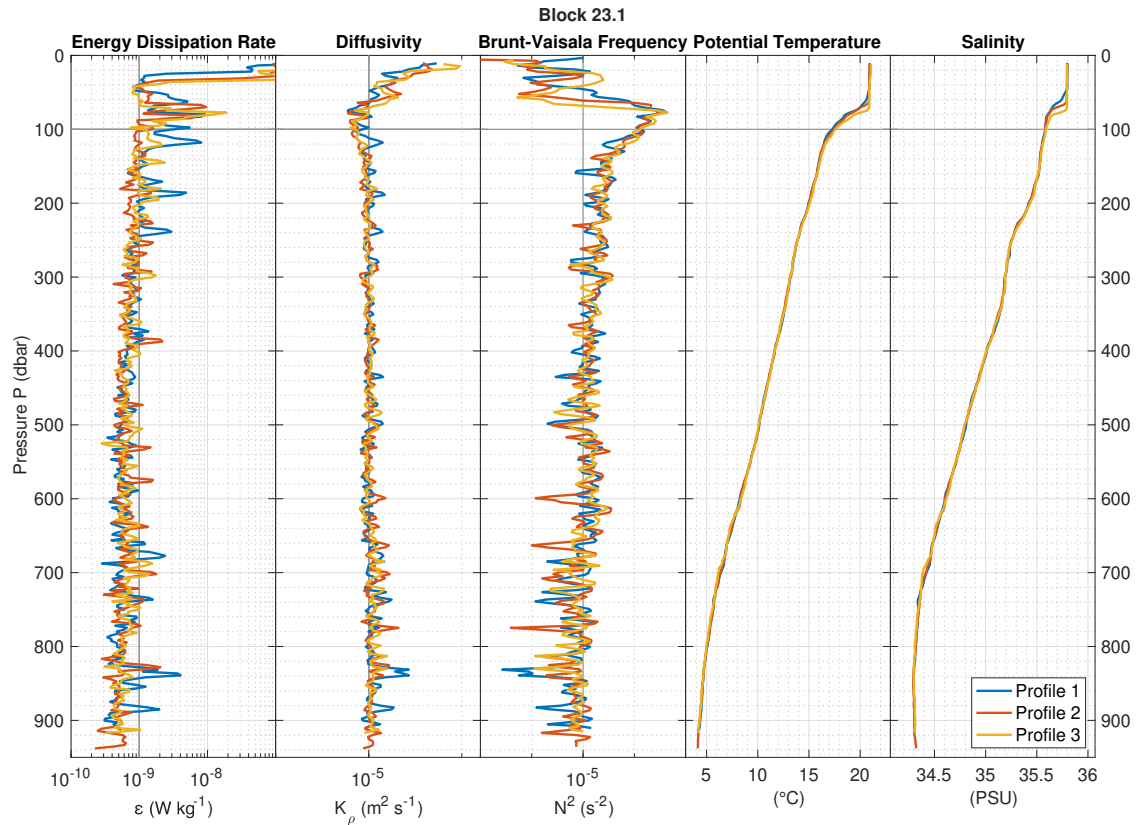
Figure 20: Energy dissipation rate, diffusivity, buoyancy frequency, potential temperature, and salinity for the three profiles measured during the first block of casts at station 23. Same colour corresponds to same profile in all plots. The horizontal gray line indicates the horizon corresponding to a pressure of 100 dbar. The vertical gray lines correspond to $\varepsilon = 10^{-9}$ W kg^{-1}, $K_\rho = 10^{-5}$ m^2 s^{-1}, and $N^2 = 10^{-5}$ s^{-2} in the first, second, and third plots from the left, respectively.

4.1.1 Profile Averaging

For each block of casts and for each station, three different mean profiles were calculated for the energy dissipation rate, using various methods for averaging: the arithmetic mean, the geometric mean and the median. For each mean estimate, the corresponding error was also obtained, using the standard deviation for the arithmetic mean, the geometric standard deviation for the geometric mean, and the standard error of the median for the median. An overview of the mean profiles of the energy dissipation rate ε for each block of casts is shown in Fig. 21. The arithmetic mean, the geometric mean, and the median are plotted.

44
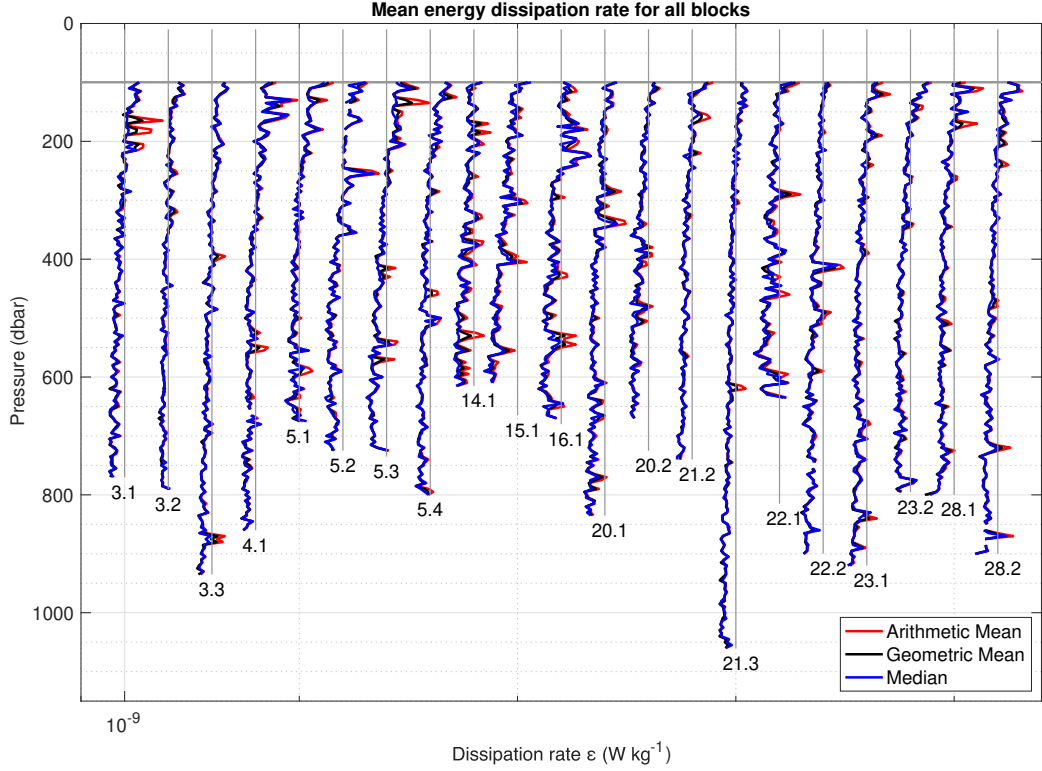
Figure 21: Mean profiles of the energy dissipation rate ε for each block of casts as a function of pressure. Profiles of different blocks, whose number is indicated at the bottom of each profile, are scaled by a factor 10. For each block, the arithmetic mean (red line), the geometric mean (black line), and the median (blue line) are shown. The horizontal dark gray line indicates the horizon corresponding to a pressure of 100 dbar. Data collected above such pressure are not shown in this plot in order to better visualize the data that were the focus of the analysis. The vertical dark gray lines always correspond to a value of ε equal to 10^{-9} W kg^{-1}. Such lines are shown in order to allow for better visualization of the results and for easier comparison between the blocks.

Fig. 22 shows, one next to the other, all the station mean profiles of the energy dissipation rate, ε. For each station, the arithmetic mean, the geometric mean, the median, and the standard deviation are plotted. It is important to underline that the station average does not come from the averaging of the mean profiles of the blocks corresponding to that station. Instead, it comes from the averaging of all the profiles contained in such blocks. This result is more accurate because it prevents the average calculation from being performed twice, which would inevitably increase the error associated with it. Nevertheless, one has to note that the number of profiles (and blocks) corresponding to a station is not the same for every station. Instead, it ranges from 3 to 11 (1 to 4). Consequently, for stations with a larger number of profiles we have a more accurate and reliable description of the average turbulence and energy dissipation. Moreover, since some

45

profiles are shorter than others (i.e. their maximum pressure is lower), the deeper we go, the higher the uncertainty associated with the mean profile can get.
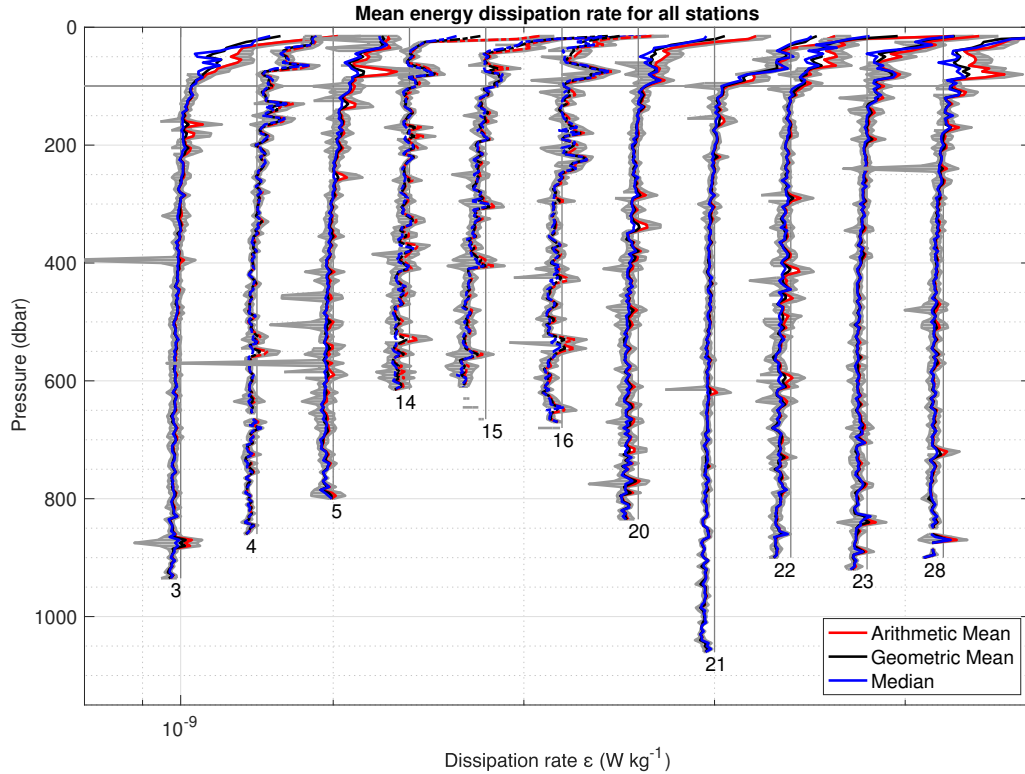
Figure 22: Stations' mean profiles for the energy dissipation rate ε as a function of pressure. Profiles of different stations, whose number is indicated at the bottom of each profile, are scaled by a factor 10^2. For each station, the arithmetic mean (red line), the geometric mean (black line), the median (blue line), and the standard deviation (gray area) are shown. When the standard deviation is so large that the estimation of the error on the arithmetic mean is bigger than the value of the arithmetic mean itself, this can not be plotted on a logarithmic scale. In fact, $\varepsilon - \delta\varepsilon$ becomes negative and it is, therefore, disregarded during the plot. This is the reason why sometimes only half of the uncertainty interval over the ε estimation is shown. The stations with the dashed lines represent those for which only one block of measurements was carried out. The horizontal gray line indicates the horizon corresponding to a pressure of 100 dbar. For our analysis, only data collected below that pressure were considered. The vertical gray lines always correspond to a value of ε equal to 10^{-9} W kg^{-1}. Such lines are shown in order to allow for better visualization of the results and for easier comparison between the stations.

When multiple blocks of casts were collected at one station, the stations' mean profiles tend to show larger ε than the blocks' mean profiles. This is due to the fact that different profiles show spikes at different pressures due to turbulence intermittency. When these profiles are averaged, the peaks are smoothed but the mean dissipation tends to increase.

46

This effect is greater the more profiles are averaged together.

The uncertainties associated with the mean epsilon profiles are quite large (more than one order of magnitude, sometimes), especially when the single profiles that are averaged differ significantly one from the other. The standard deviation is sometimes bigger than the ε estimation itself and, therefore, this can not be plotted in a logarithmic scale since negative values are ignored in the plot. The arithmetic mean gives a result that is the most dependent on spikes present in single profiles. This can be clearly seen in Fig. 23, where all the profiles measured at station 3 are plotted three times, in three different plots. In each plot, a different averaging of the profiles is shown, respectively the arithmetic mean, geometric mean, and median.
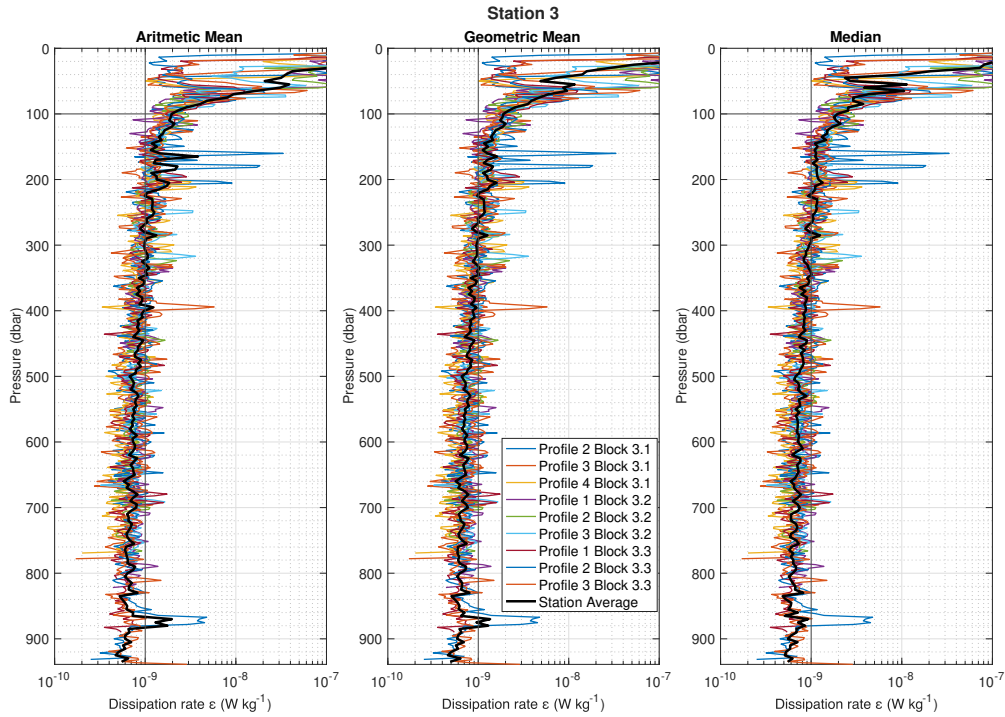
Figure 23: Energy dissipation rate ε profiles measured at station 3 as a function of pressure. In the plot on the left, the station average (black thick line) is calculated using the arithmetic mean. In the plot in the centre, the station average (black thick line) is calculated using the geometric mean. In the plot on the right, the station average (black thick line) is calculated using the median. The horizontal gray line in each plot indicates the horizon corresponding to 100 dbar. The vertical dark gray lines correspond to 10^{-9} W kg^{-1}. Same colour corresponds to same profile in all plots.

Profile 2 from Block 3.1 shows three very evident spikes between 150 and 200 dbar. These are evident also in the station average obtained using the arithmetic mean (Fig. 23, left). On the other hand, only some fluctuations are visible in the average profile if one uses

the geometric mean (Fig. 23, centre). In the same pressure interval, the median profile is relatively constant (Fig. 23, right). Compared to the other averages, the arithmetic mean tends to be more dependent on a single profile showing extremely high values and less dependent on all other profiles that do not show them.

4.1.2 Depth Integrated Dissipation ϵ

The cumulative depth integrated dissipation profiles of all the stations are shown in Fig. 24, together with the corresponding stations' mean ε profiles, for a better comparison.
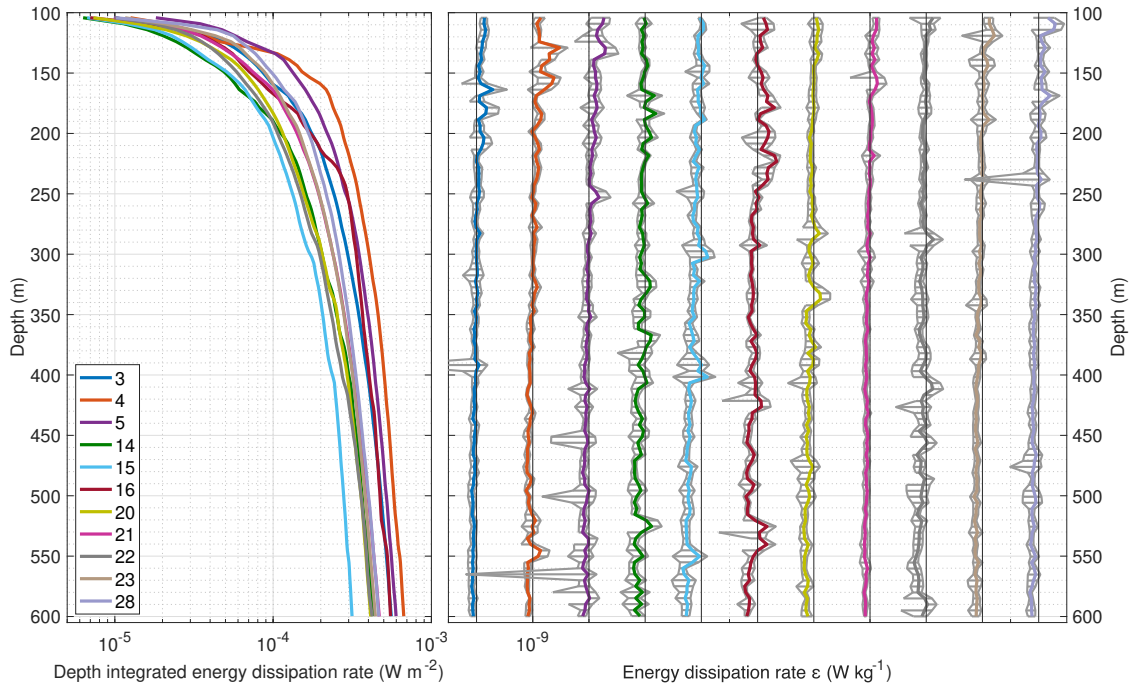
Figure 24: Left: cumulative depth integrated mean energy dissipation rate at every station, from 100 to 600 m depth. Right: (arithmetic) mean energy dissipation rate profiles at every station, with standard deviation (gray lines), from 100 to 600 m depth. Same colour corresponds to same station in both plots. Profiles of different stations are scaled by a factor 10^2. When the ε arithmetic mean is smaller than its uncertainty, only half of the error bar can be plotted due to the logarithmic scale. The vertical gray lines always correspond to $\varepsilon = 10^{-9}$ W kg^{-1}.

For each station, the last value (hence, corresponding to a depth of 600 m) of the cumulative depth integrated dissipation is the depth integrated energy dissipation rate (ϵ) corresponding to that station. The so obtained ϵ are summarized in Table 7 and plotted on a map in order to visualize each result at its exact location (Fig. 25). The greatest values are found at stations 3, 4, 5 and 16, but by observing the average epsilon profiles (for example in the right panel of Fig. 24) this trend is not easily or clearly identifiable.

Station Number	$\epsilon \cdot 10^{-3}$ (W m^{-2})	Station Number	$\epsilon \cdot 10^{-3}$ (W m^{-2})
3	0.5575229	20	0.4135337
4	0.668898	21	0.4682885
5	0.5979769	22	0.4216278
14	0.4292055	23	0.4426814
15	0.3151604	28	0.4646289
16	0.5516229		

Table 7: List of stations and corresponding depth integrated energy dissipation rate (ϵ).
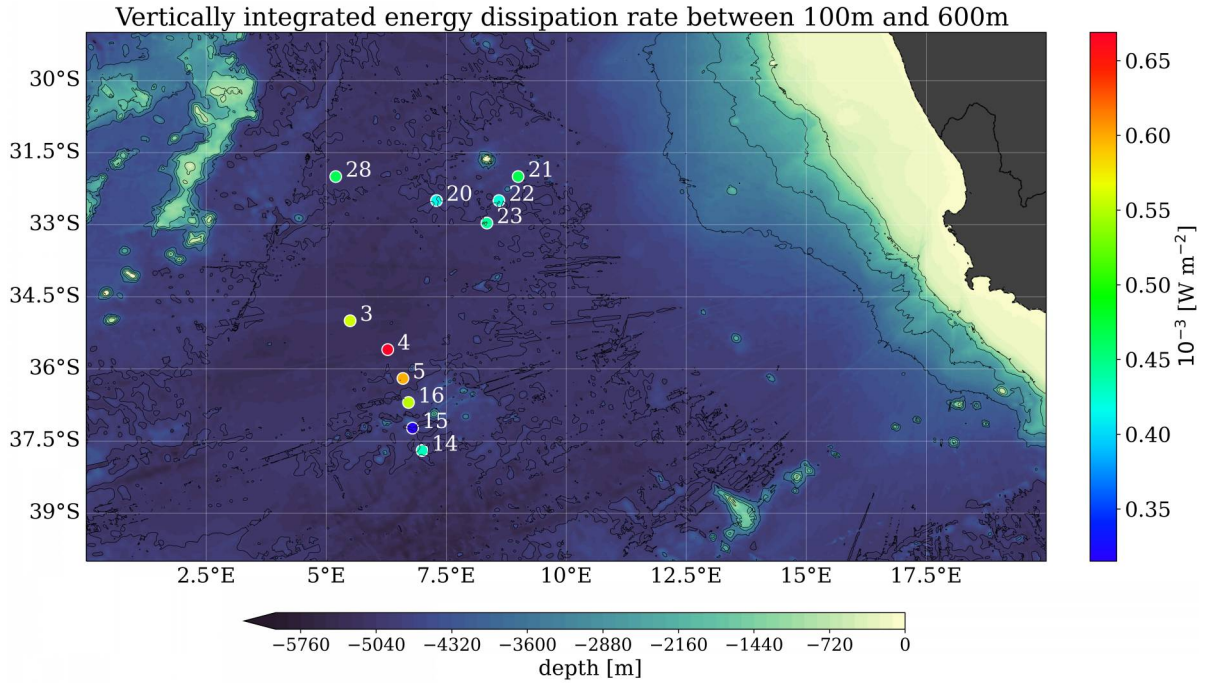
Figure 25: Depth integrated energy dissipation rate (ϵ) at each station's location on a map of the Southern Atlantic Ocean. The colour of each dot is proportional to the corresponding value of ϵ. The stations' numbers, the ocean bathymetry, and part of the African continent are also shown.

From now on, for clearness, the depth integrated dissipation of single profiles will be indicated with the symbol ϵ_p. Other integrations with depth were performed for every profile: one (ϵ_b) for the smooth "background" curve, one (ϵ_1) for a single notable spike in the ε profile between 100 and 300 m and one (ϵ_2) for a single notable spike in the ε profile between 300 and 600 m. For each profile, three ratios were calculated: the ratio ($R_b = \epsilon_b/\epsilon_p$) of the depth integrated dissipation "background" and ϵ_p, the ratio

($R_1 = \epsilon_1/\epsilon_p$) of the integral of the chosen dissipative events between 100 and 300 m and ϵ_p, and the ratio ($R_2 = \epsilon_2/\epsilon_p$) of the integral of the chosen dissipative events between 300 and 600 m and ϵ_p. All the results are listed in Table 11 in Appendix B. These ratios correspond to the percentage contributions to ϵ_p of the small-scale mixing and of the selected dissipative events, respectively. By averaging the percentages of all profiles, it was found that the dissipation caused by small turbulent events (that could not be identified) contributes by $84\% \pm 9\%$ to the total dissipation, while, on average, the largest spike (or one of the largest) between 100 and 300 m and the largest spike (or one of the largest) between 300 and 600 m make up $8\% \pm 6\%$ and $6\% \pm 7\%$, respectively, of the total dissipation. Hence, the energy dissipation produced by other turbulent events corresponds to only around 2% of the total dissipation of energy between 100 and 600 m.

4.1.3   Evaluation of the amount of total dissipated energy

When calculating the total amount of energy dissipated by the internal wave field inside the study area, I obtained:

$$\overline{\sigma} \cdot \overline{\varepsilon} \cdot V_{study} = 0.1 GW = 10^8 W$$

where $\overline{\sigma}$ is a mean constant density, $\overline{\varepsilon}$ a mean energy dissipation rate, and V_{study} the volume of the considered study area. We can compare this result with the energy dissipated in total by internal waves in the whole ocean basin (0.2 TW [Munk and Wunsch (1998)]). In the area where we performed the VMP deployments, the energy dissipated by internal waves is about 1/2000 of the total energy dissipated by internal waves in the entire ocean.

4.1.4   Calculation of energy dissipation rates from Thorpe Scale

For each one of the 62 valid profiles, an energy dissipation rate profile using density inversions, i.e. the method introduced by Thorpe (1977), was computed. Such profiles, in general, show stronger fluctuations than the ones measured by the shear probes of the VMP. Fig. 26 shows on the left ε_T as a function of pressure for all the profiles of block of casts 2, station 3, and on the right the dissipation profiles obtained from the shear probes (ε), during the same cast. A more consistent and direct comparison is possible in the left panel of Fig. 27, where ε_T and ε_O (i.e. the energy dissipation rate directly measured and then interpolated in each turbulent patch) are shown as a function of depth for the second profile of block of casts 1, at station 5.
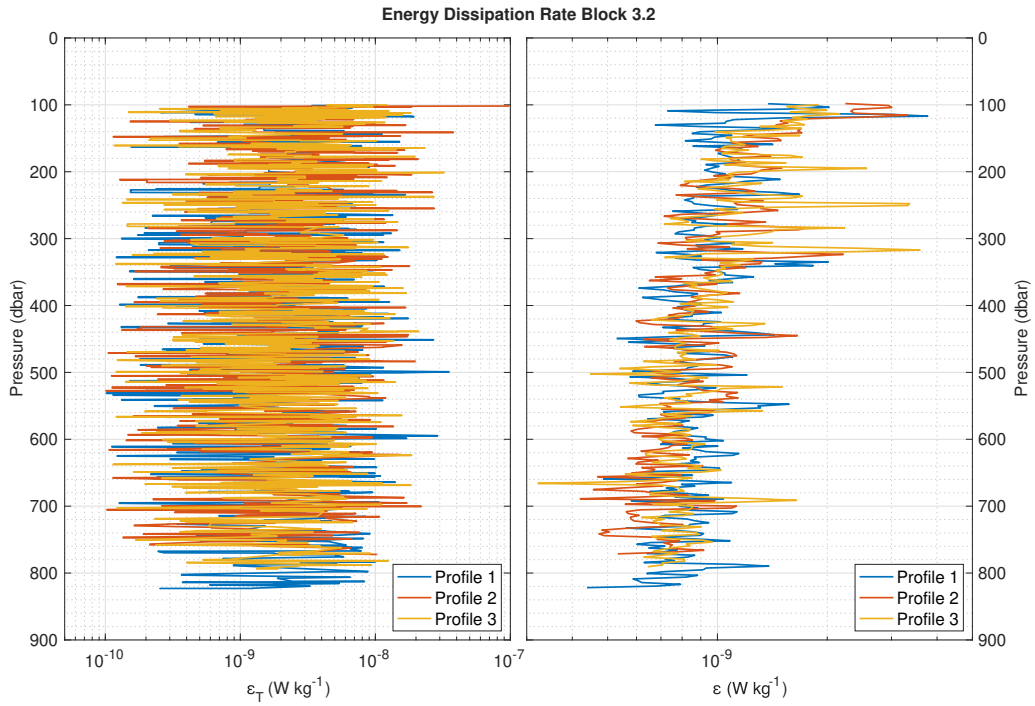
Figure 26: Left: energy dissipation rate obtained from the water parcels overturns (ε_T) as a function of pressure. Right: energy dissipation rate estimated from shear probes (ε) as a function of pressure. Note that while ordinates of the two plots are the same, the abscissa scale changes.
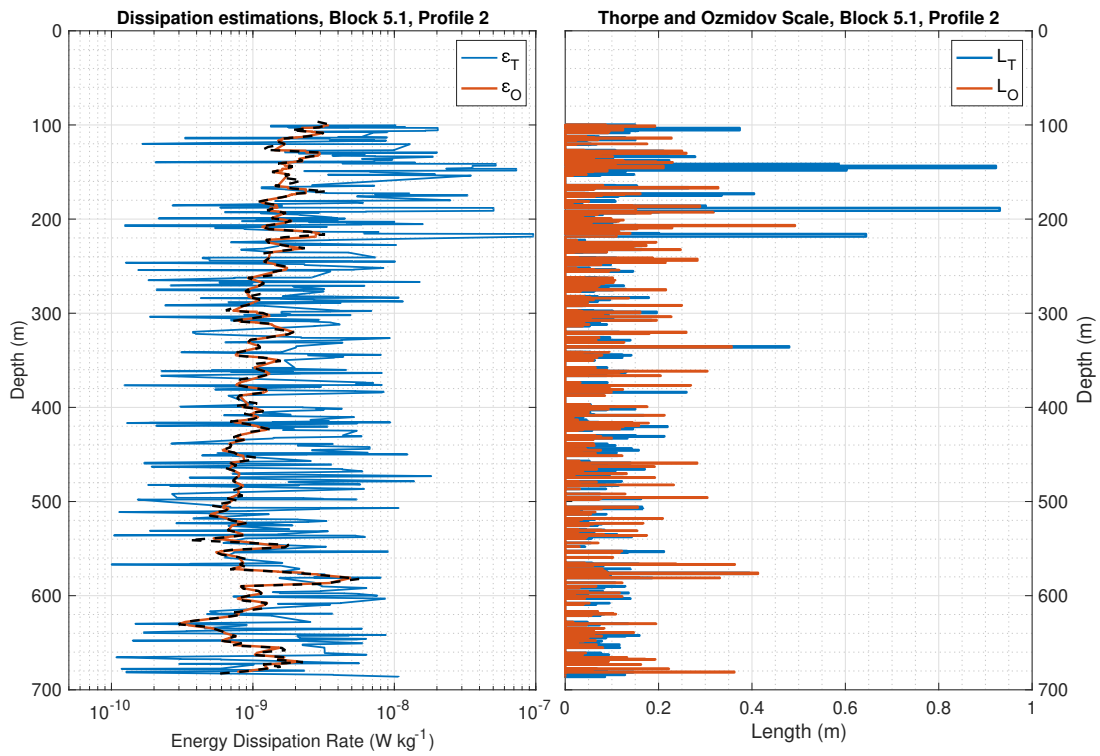
Figure 27: Left: dissipation obtained from water parcels overturns (ε_T) and from shear probes data, interpolated in each turbulent patch (ε_O). Right: Thorpe scale estimated from displacements and Ozmidov scale calculated inserting ε_O into Eq. 4.

The fact that ε_T tends to be larger than ε_O can be partly explained by the fact that the estimations of the Thorpe Scale tend to be larger than those of the Ozmidov Scale. This is clear if one directly compares the magnitude of L_T (used for the calculation of ε_T) and that of L_O, obtained from the individual profiles of ε_O, by using Eq. 4. This is shown in the right panel of Fig. 27 for station 5, block of casts 1, profile 2. L_T and L_O are constant over one turbulent patch and their relative magnitudes are, overall, quite similar. Some peaks for L_T, which are likely to be unreliable, stand out, especially between 100 and 300 dbar, and cause some ε_T estimates to be larger than ε_O estimates.

In order to compare all data for L_T and L_O at the same time, a scatter plot of $log(L_T)$ vs $log(L_O)$ is shown in Fig. 28. Moreover, the same figure illustrates a histogram of all values of $log(L_T/L_O)$ with a normal density function fit.
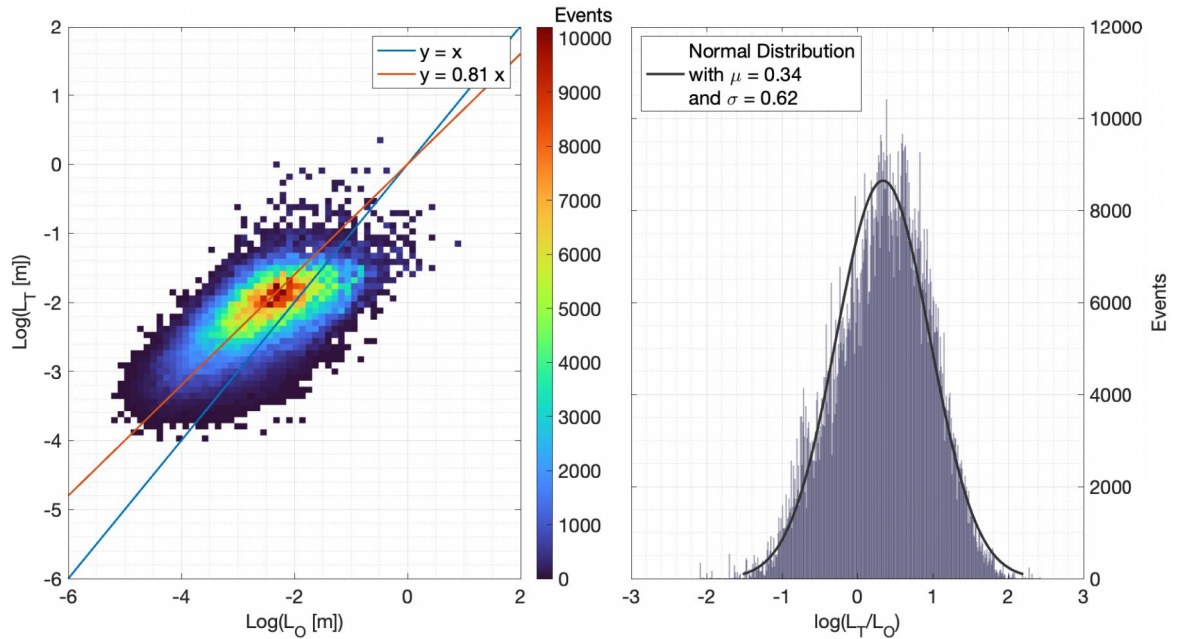
Figure 28: Left: scatterplot comparisons of Thorpe L_T and Ozmidov L_O scales calculated from turbulent patches for all 11 stations. Point density is represented by the colour bar. The 1 to 1 line (blue line) and the function (with intercept set to zero, orange line) best interpolating the point density are shown. Right: logarithmic ratio of ordinate to abscissa ($log(L_T/L_O)$) for all turbulent patches in the 11 stations. A fit with a normal density function is performed and shown (black line) and some measures of central tendency (the parameters of the normal distribution) are indicated.

On the other hand, from the mean of the L_O/L_T ratio, a new value for the proportionality constant between L_T and L_O (see Eq. 6) was estimated:

$$a' = 0.87 \pm 0.62$$

and used for calculating new estimates for ε_T (that I named ε_T'). For every station, all the

single profiles of both ε'_T and ε were averaged as a function of density and the resulting mean profiles ($\overline{\varepsilon'_T}$ and $\bar{\varepsilon}$) are shown in Fig. 29.
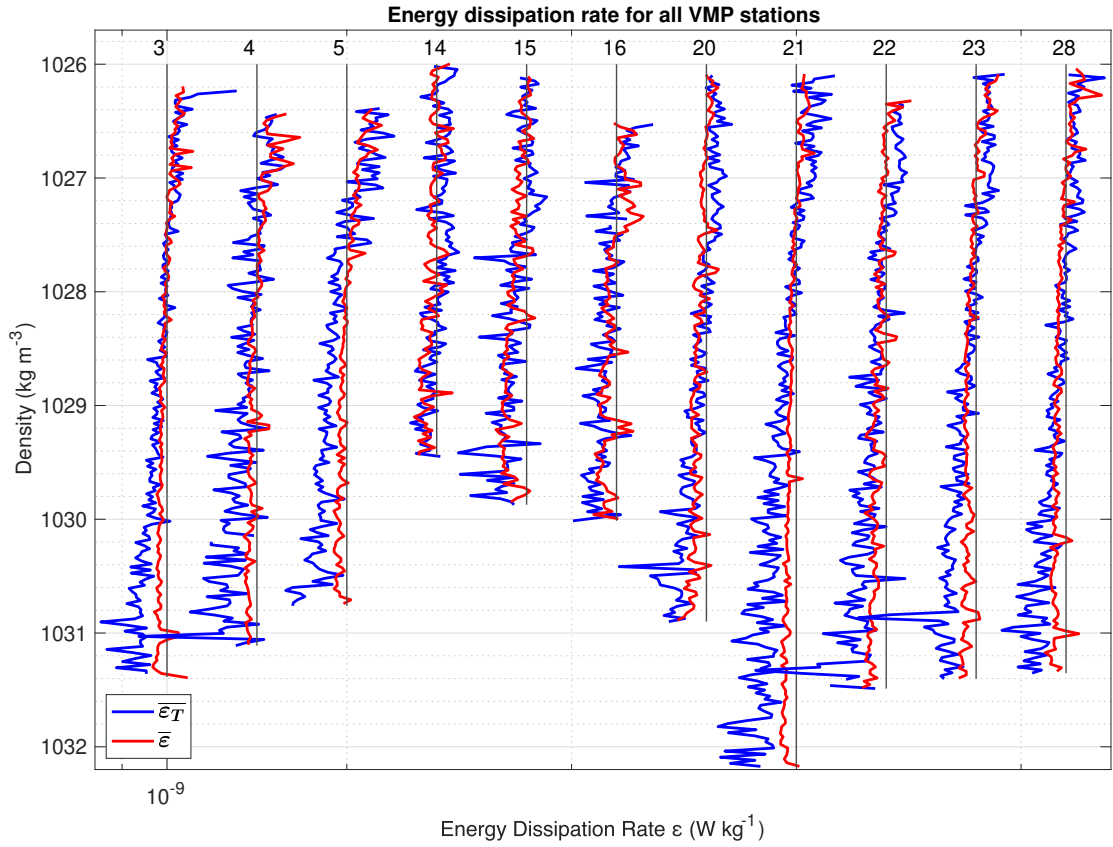
Figure 29: Stations' mean dissipation profiles, obtained using different methods, as a function of density. The turbulent kinetic energy dissipation rate profiles were estimated from Thorpe scales using the previously calculated proportionality constant a' (blue lines), or directly measured by shear probes (red lines). Profiles of different stations, whose number is indicated at the top of each profile, are scaled by a factor 10^2. The vertical dark gray lines always correspond to a value of ε equal to 10^{-9} W kg^{-1}, allowing for better visualization and comparison.

4.2 MR

4.2.1 Depth Integrated Dissipation ϵ

For each MR profile, the last value (hence, corresponding to a depth of 600 m) of the cumulative depth integrated dissipation is the depth integrated energy dissipation rate (ϵ) corresponding to that profile. The so obtained ϵ are plotted on a map in order to visualize each result at its exact location (Fig. 25) and summarized in Table 13 in Appendix D.
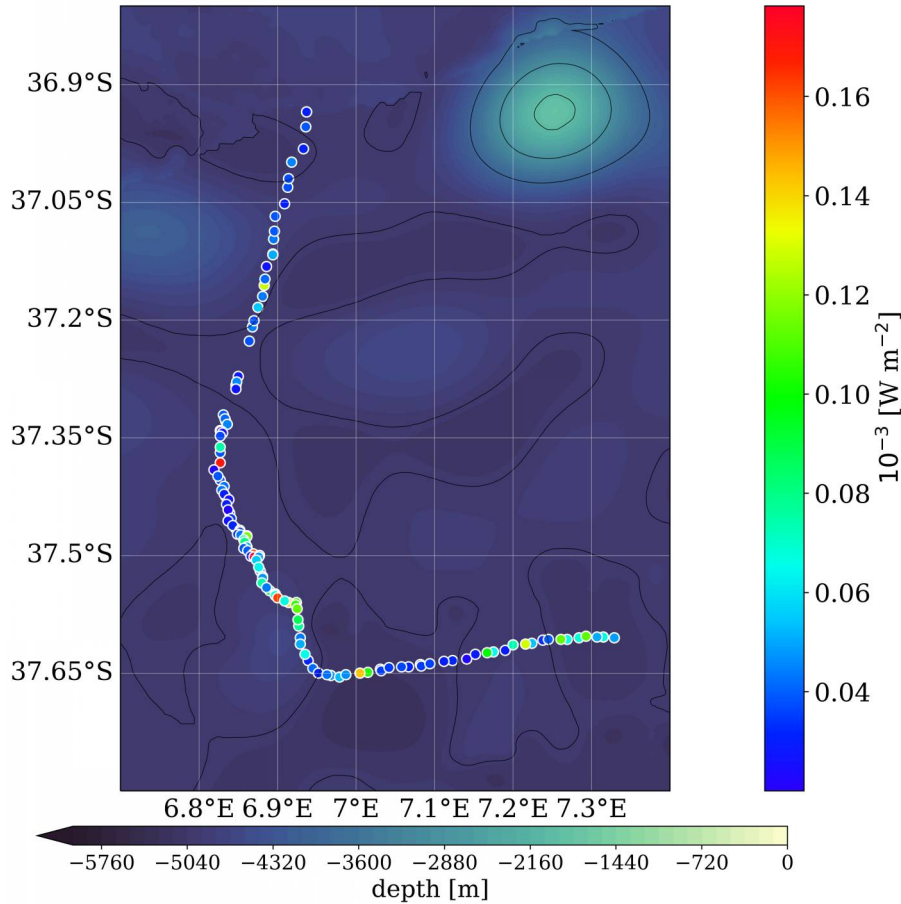
Figure 30: Depth integrated energy dissipation rate (ϵ) at each MR profile's location on a map. The colour of each dot is proportional to the corresponding value of ϵ. The ocean bathymetry is also shown.

For consistently comparing ϵ values computed from VMP profiles and from MR profiles, $\varepsilon < 10^{-10}$ from MR profiles are discarded before calculating ϵ again. Since MR profiles were collected in a relatively small area, it makes sense to group them, in order to look for spatial dependence in ϵ estimates. The newly calculated ϵ of all MR profiles, divided into six non-equisized subareas (see Table 8), were averaged, and the so-obtained mean depth integrated dissipations $\bar{\epsilon}$ are shown on a map in Fig. 31, together with the depth integrated energy dissipation rate for each VMP station. The mean depth integrated dissipations obtained from MR data are relatively smaller than the ones obtained from VMP data. This is due to the fact that MR profiles show a much weaker dissipation than VMP profiles. This is clearly visible in Fig. 32 where the VMP arithmetic mean profile at station 14 is compared with the arithmetic mean of the three MR profiles (profiles 101, 102, and 103) that were collected closest to station 14.

Sub--area	Lat$_{min}$ (°S)	Lat$_{max}$ (°S)	Lon$_{min}$ (°E)	Lon$_{max}$ (°E)	Number of profiles	$\bar{\epsilon} \cdot 10^{-4}$ ($\frac{W}{m^{-2}}$)
A	36.90	37.10	6.89	6.94	11	1.0
B	37.10	37.30	6.84	6.90	14	1.2
C	37.30	37.50	6.81	6.87	42	1.2
D	37.50	37.70	6.86	7.00	33	1.4
E	37.62	37.66	7.00	7.16	14	1.1
F	37.60	37.63	7.16	7.34	15	1.3

Table 8: Subareas in which MR profiles were grouped, the geographical coordinates of their edges, the number of profiles collected inside each subarea, and the mean depth integrated dissipation $\bar{\epsilon}$.
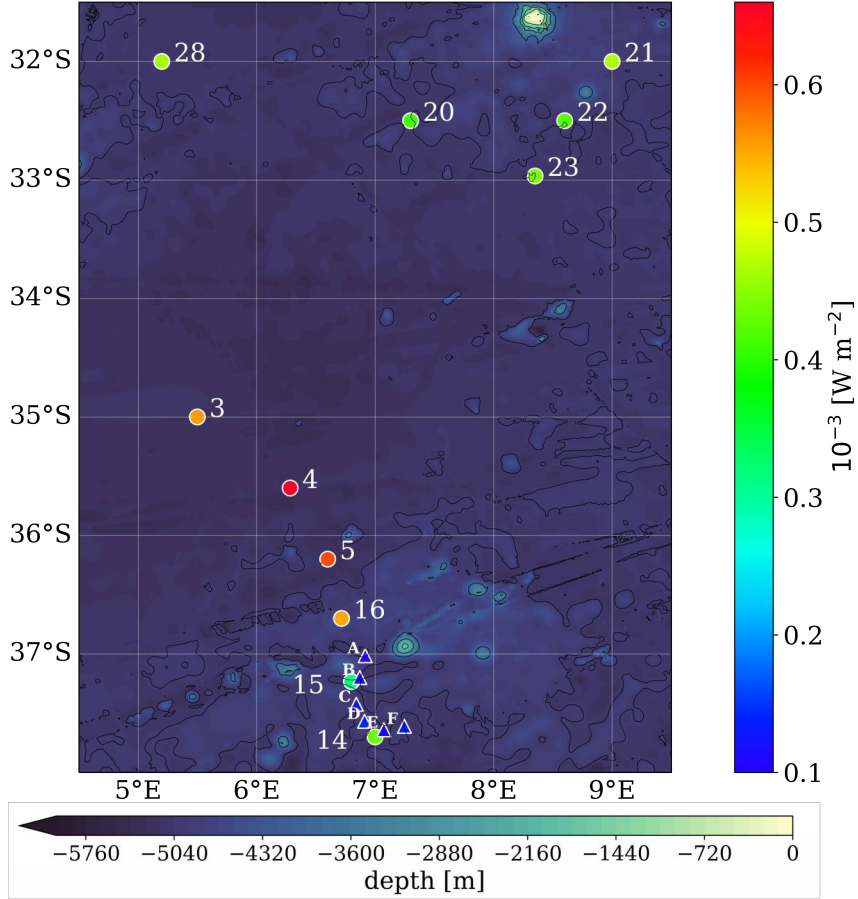
Figure 31: Mean depth integrated energy dissipation rates ($\bar{\epsilon}$) of the six MR subareas and of the eleven VMP stations. The results are plotted at their location (calculated as the arithmetic mean of the coordinates of all averaged profiles) on a map of the Southern Atlantic Ocean. The colour of each dot is proportional to the corresponding value of the depth integrated dissipation. The ocean bathymetry is also shown.
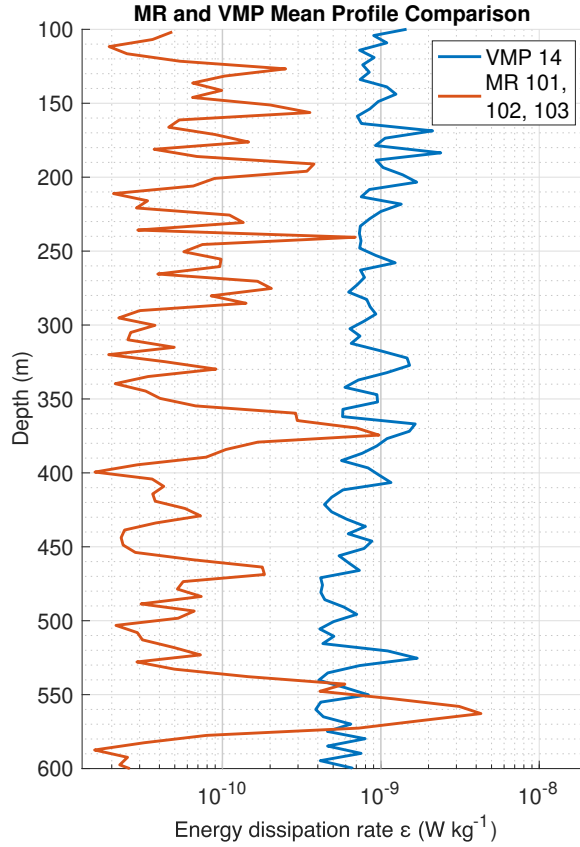
Figure 32: Energy dissipation rate profiles measured by the VMP and by the MR at very close locations. The VMP estimation (blue line) is the arithmetic mean of the profiles collected at station 14. The MR estimation (orange line) is the arithmetic mean of three MR profiles: 101, 102, and 103. The depth range that is plotted is the one that was integrated for the calculation of ϵ.

For the MR, the mean over all 129 profiles of the ratio between the integral of the smoothed dissipation curve and the integral of the measured profile gives 0.47 ± 0.15. This contribution of the "background" to the total dissipation is much smaller that the one obtained from the VMP data (0.84 ± 0.9). Nevertheless, this result is reasonable considering that the MR mounted on a glider, compared to the VMP, is sensitive to much lower ε values and it is able to resolve turbulence at a smaller scale.

5 Discussion

5.1 VMP

Some blocks of casts do not show particularly interesting features (for example block 3.2) in the temperature and salinity profiles, while others, such as block 5.4, present more notable variations that often disappear in the density profiles. By visually comparing the density anomaly profiles (not shown) and the ε profiles measured with the shear probes, it is not possible to notice any outstanding correlation between peaks of turbulence and density fluctuations. The dissipation profiles can be characterised by rapid fluctuations, like in block 23.1, or by wider spikes, as in block 5.4, but all tend to show a decrease in ε from $\sim 10^{-9}$ at the bottom of the mixed layer to $< 10^{-9}$ deeper than 300 dbar, excluding the peaks caused by strong dissipative, turbulent events. Overall, the measured dissipation shows values that are of the expected orders of magnitude ($10^{-10} - 10^{-9}$). The same is true for the calculated buoyancy frequency ($N^2 \sim 10^{-5}$) and diffusivity. In fact, mixing is attributed to widespread diapycnal diffusivity of $K_\rho = 10^-5$ m^2 s^{-1} from breaking internal waves.

In conclusion, after having observed all the profiles, it can be stated that different blocks have different characteristics but that, especially as regards the dissipation profiles, none of these is unique or has particularly relevant anomalies. This is the reason why the division in the different study areas (eddy, beam, and smeso) was not significantly used during the description of the results: it turned up not to be useful nor relevant for the distribution of dissipation rates.

5.1.1 Profile Averaging

The magnitude of the energy dissipation rate can be misidentified due to its erratic evolution when working with observational data. Previous studies have often employed either arithmetic averaging (e.g. Dillon (1982)), which conserves energy, or geometric averaging (e.g. Ferron et al. (1998)), which seems effective for a log-normal population. Unfortunately, no clear reasoning exists about the appropriate method of averaging observed energy dissipation rates [Sugiura et al. (2018)]. Compared to the arithmetic mean, the geometric mean tends to be less dependent on a single profile showing extremely high values, while all other profiles do not. On the other hand, the median seems to be a good estimation for the background state since it underestimates turbulent events.

The block mean profiles for ε show a trend similar to that of the single profiles: ex-

cluding the peaks of the dissipative, turbulent events, ε is $\sim 10^{-9}$ from the bottom of the mixed layer to about 300 dbar and $< 10^{-9}$ at deeper pressures. Moreover, no particular feature can be observed in any of the mean profiles.

5.1.2 Depth Integrated Dissipation ϵ

As one can see in Table 7 and in Fig. 25, the depth integrated energy dissipation rate, ϵ, varies at most by a factor of 2 between the various stations, so the different positions show very similar values after all. It seems that the stations located in the beam study region (20, 21, 22, 23, and 28) are characterized by medium-low (and similar to each other) ϵ. On the other hand, in the stations of the eddy study region (3, 4, and 5) and smeso study region (14, 15, and 16), the ϵ values show greater variations, including the highest and the lowest result obtained here for the depth integrated dissipation. Furthermore, it can be observed that ϵ tends to be relatively high in the eddy study area, but it is not possible to draw conclusions given the overall limited number of stations and the small difference between ϵ estimates. It is more prudent to conclude that there is not much difference between the various positions: a result already suggested by the various (measured and averaged) dissipation profiles.

When looking at the depth integrated energy dissipation rate of single profiles (ϵ_p), it is interesting to evaluate how much of this dissipation was due to the small-scale dissipation and how much was due to the resolved mixing events. I estimated that the dissipation caused by unidentifiable turbulent events is, on average, $84\% \pm 9\%$ of the total energy dissipation, while the one due to identified turbulent events is only about $16\% \pm 13\%$ of the total dissipation. This is an interesting result because it implies that, from any single ε cast, it is possible, by integrating a smooth version of the measured profile, to estimate a depth integrated dissipation value that is about 84% of the actual dissipation of energy taking place at that location. The measure (and resolution) of the transient dissipative events, making up only about 16% of the total energy dissipation, is not so necessary or determinant when estimating the average total amount of energy dissipated in a region of interest. Hence, fewer deployments per station might be needed.

5.1.3 Evaluation of the amount of total dissipated energy

In our VMP study area, in the ocean layer between 100 and 600 dbar, 0.1 GW $= 10^8$ W are dissipated. This might seem a small number, compared to the 0.2 TW $= 2 \cdot 10^{11}$ W [Munk and Wunsch (1998)] dissipated world-wise by the internal wave field. However,

the total volume of the ocean is more than 10^4 times bigger than the volume of water considered in our calculation. Therefore, we can conclude that this area, even though it does not show outstanding, strong turbulence, contributes in a relatively considerable way to the dissipation of energy in the ocean through mixing caused by internal waves. In fact, the mean energy dissipated energy for this area, $\bar{\varepsilon}$, is 6 times larger than the ocean average dissipation rate of $\varepsilon_{ocean} = 1.5 \cdot 10^{-10}$ W kg^{-1}. This is due to two reasons. The first one is the depth interval taken into account: the integration was performed between 100 and 600 m, the upper part of the ocean interior, but gradients and turbulence decrease in the abyss. Hence, ε is also smaller in the deeper layers. The second reason for this relatively high rate of turbulent energy dissipation is the location: the expedition took place southeast of the Walvis Ridge. Ocean ridges are major stirring rods in ocean basins, where, on the contrary, background mixing is usually moderate or weak.

5.1.4   Calculation of energy dissipation rates from Thorpe Scale

One of the main goals of this thesis was to estimate energy dissipation rates in the study region using two different methods and comparing them. What I obtained is that the single profiles of ε_T (the dissipation obtained from density inversions) show more, and more prominent, fluctuations, compared to the dissipation directly measured. In general, ε_T profiles span multiple orders of magnitude. Some high values of ε_T, especially between 100 and 300 dbar, are due to high values of L_T (especially if compared with those of L_O). This is, nevertheless, consistent with the assumptions and requirements of the method introduced by Thorpe. Such method is not suitable nor reliable for calculating a single dissipation profile. It can also not be used for accurately estimating single ε values and resolving individual dissipative events. Instead, it is useful for a statistical study of turbulence caused by the breaking of internal waves and for the estimation of the average dissipation rate profile in a specific area. In fact, a large amount of data is usually required to successfully apply this method. Overall, the estimated values for L_T in this study are satisfying, as demonstrated by the results obtained from the statistical comparison between L_T and L_O, where all our data were simultaneously included. As in Mater et al. (2015), the scatterplot comparison of the Thorpe L_T and Ozmidov L_O scales in the left panel of Fig. 28 shows a data cluster near $L_T \sim L_O$, but with some more scatter than reported by Dillon (1982). The best linear regression (with intercept set to zero) for our data gives a slope equal to 0.81. Moreover, as expected, I found that L_T/L_O is lognormally distributed (see right panel of Fig. 28). Such log-normal behaviour was reported by

Stansfield et al. (2001) and Mater et al. (2015), among others. The mean of the L_O/L_T ratio gives the proportionality constant $a = 0.87 \pm 0.62$. Such value is consistent with what other studies calculated. Some are listed in Table 9.

Author	Location	Relation $L_O = a \cdot L_T$
Dillon (1982)	Seasonal oceanic thermocline	$L_O = 0.79(\pm0.40) \cdot L_T$
Ferron et al. (1998)	Ocean T< 2°C	$L_O = 0.95(\pm0.60) \cdot L_T$
Mater et al. (2015)	Luzon Strait	$L_O = 1.09(\pm0.07) \cdot L_T$
This work	Southeast of the Walvis Ridge	$L_O = 0.87(\pm0.62) \cdot L_T$

Table 9: Studies of the linear relation between the Ozmidov scale and the Thorpe scale with their results for the proportionality constant a and its uncertainty.

Overall, the stations' mean profiles, $\overline{\varepsilon'_T}$ and $\overline{\varepsilon}$, shown in Fig. 29 as a function of density, agree for all stations, especially up until a density of about 1030 kg m^{-3}. At densities higher than 1030 kg m^{-3}, i.e. deeper in the ocean, $\overline{\varepsilon'_T}$ profiles tend to decrease and become significantly lower than $\overline{\varepsilon}$ profiles. This is mainly caused by the fact that for calculating $\overline{\varepsilon}$ I averaged fewer but higher data (ε), while for the estimation of $\overline{\varepsilon'_T}$ I considered also many $\varepsilon_T = 0$, especially in the deep ocean. In fact, with the shear probes we were not able to measure any $\varepsilon < 10^{-10}$ W kg^{-1}, and there is, in any case, a threshold value for the dissipation that one can estimate, given by the noise level of the VMP. On the other hand, using the Thorpe Scale I necessarily individuate layers to which a dissipation equal to zero ($\varepsilon_T = 0$) was attributed. These are the stable parts of each profile, where $L_T = 0$. Such ε_T are then taken into account when averaging individual profiles as a function of density, lowering the mean dissipation. Having obtained $\varepsilon_T = 0$ in a layer does not necessarily mean that, in reality, there is no dissipation going on in that layer. On the contrary, there is always an infinitesimal dissipation of energy taking place. However, estimations of $L_T = 0$ do tell us that the water column there is particularly stable and very little turbulence, and thus little dissipation of energy, was occurring. This information is relevant and, therefore, I decided not to neglect values of $\varepsilon_T = 0$ when averaging, even though they significantly affect the resulting $\overline{\varepsilon'_T}$ profiles at densities larger than 1030 kg m^{-3}, where the density gradient is lower and $L_T = 0$ is more frequent. A solution for this limitation of Thorpe's method could be to use different threshold values (for identifying density inversion in the intermediate density profiles) in different layers, depending on how steep the density gradient is in that layer. It is worth noticing that the VMP was equipped with a compact CT that samples data at 64 Hz, but standard CTD have a

much lower sampling rate (24 Hz). This means that fewer, yet more accurate data are collected, making it possible to use L_T to estimate dissipation in the deep ocean. The final purpose of Thorpe's method is to use data collected with CTDs to calculate dissipation because such data are relatively accessible in comparison to measurements that require microstructure shear profilers. Looking at my results, we can conclude that below the pycnocline, this method appears to be appropriate until the depth at which it starts to be hard (with the CTD that is being used) to note and accurately determine inversions in the density gradient. On the other hand, if one wants to study the microstructure features of dissipation and of the related phenomena and wants to be able to resolve individual turbulent events with reliability and precision, then instruments, such as the VMP or the MR, are needed.

5.2   MR

5.2.1   Depth Integrated Dissipation ϵ

As for the VMP, it appears that the depth integrated energy dissipation rate, ϵ, obtained from MR data, does not differ significantly inside the region where the glider travelled. Moreover, the majority of ϵ estimates are between $0.02 \cdot 10^{-3}$ and $0.04 \cdot 10^{-3}$ W m^{-2}. The values for ϵ, obtained from MR profile, are always relatively lower than those obtained from VMP profiles. This tendency persists also when multiple profiles are averaged together, as I did for the stations' mean in the case of the VMP and for the subareas' mean in the case of the MR. Even though it is true that the MR has a lower noise level than the VMP, this reason alone does not explain the big discrepancy (of about one order of magnitude) between the magnitude of the ε profiles measured by the MR and those measured by the VMP. One hypothesis, which has not been further investigated during the realization of this work, is that the disagreement is caused by the fact that, for the two instruments, different parameters were used for calculating ε and inconsistent approaches applied for the validation of the dissipation estimates.

The contribution of the unidentified turbulent events to the total dissipation in the MR profiles is about 4/7 of that in the case of the VMP profiles. This can be explained by the fact that the MR can resolve much smaller dissipation values.

In conclusion, I think that it is not appropriate to compare the ε estimates for these two datasets, as they are at the moment. In fact, I believe that they differ due to a systematic error or a methodological bias.

6   Summary and Conclusion

Diapycnal mixing in the region southeast of the Walvis Ridge, in the eastern South Atlantic, has been examined using microstructure and finestructure data from a VMP and a MR. The focus was on ocean layers deeper than the mixed layer, from a minimum pressure of 100 bdar to a maximum of 1000 dbar. Instrumentation aboard the VMP provides direct estimates of the energy dissipation rate ε and corresponding measurements of pressure, conductivity and temperature. For each one of the 62 collected profiles, a big range of variables was visualized and carefully analyzed, such as the energy dissipation rate, eddy diffusivity, buoyancy frequency, potential temperature, salinity, and density anomaly. Despite the individual peculiarities of each profile, for example the presence in some of them of a signature presumably attributable to internal wave breaking, none showed exceptional uniqueness. The energy dissipation rate and diffusivity profiles collected during the numerous deployments of the VMP are all of the same, expected, order of magnitude: 10^{-9} W kg^{-1} and 10^{-5} m^2 s^{-1}, respectively.

In the study of ocean energetics and its budget, it is important to determine how turbulent energy dissipates on a large spatial scale and climate time scale. Different types of profile averaging inside each VMP station were performed, and it was found that, compared to the arithmetic mean, the geometric mean is less dependent on the spikes of the single profiles, while the median is usually a smooth profile. It seems to be a good estimation for a state where no big dissipative events occur. The stations' mean profiles were compared and no relevant difference was identified in the energy dissipation at the various locations. The depth (from 100 to 600 m) integrated energy dissipation rate (ϵ) at each station was also calculated and, again, the results are very similar and do not make it possible to identify any defined spatial pattern. For the VMP data, the mean of the ratio of the integral of a smooth version of every single ε profile to the integral of the single ε profile itself gave 0.84 ± 0.09. We interpreted this result as the fact that, on average, the dissipation caused by turbulent events that can not be detected with the VMP is about $84\% \pm 9\%$ of the total dissipation at that location. In case this result is confirmed by future studies, it means that if one is only interested in the average energy dissipation, and not in resolving individual dissipative events, then collecting more than a couple of profiles is not needed, saving money and time.

Furthermore, other ε profiles (named ε_T) were estimated indirectly, from Thorpe scale profiles, which were in turn calculated from finescale density inversions in the water column. From comparing estimates of the Ozmidov scale (L_O) and Thorpe scale (L_T), it

was obtained that, in this work, they are related by: $L_O = 0.87(\pm0.62) \cdot L_T$. Differences between the estimates of L_T and those of L_O are sometimes very large, which illustrates the statistical character of the relation between the Ozmidov scale and the Thorpe scale. This relation, similar to that obtained by other studies, has allowed us to estimate the dissipation rates of the turbulent kinetic energy once again. One of the limitations of Thorpe's method is that when $L_T = 0$, the estimated dissipation is also zero, but, in reality, it is simply low, due to a low density gradient, and should not be neglected. Another downside is the potential for wrongly counting salinity-compensated temperature inversions as density overturns.

While single profiles differ significantly, the station mean profiles of dissipation, directly estimated from microstructure and indirectly calculated from L_T, are similar, especially where the density gradient can be accurately measured by the CTD and the true scale of dissipation can be resolved by the VMP. This shows that a suitable averaging can considerably reduce the dispersion in the relationship between L_O and L_T obtained from individual turbulent patches, and can lead to meaningful estimates of the energy dissipation. This satisfying result validates the use of the Thorpe scales to infer the turbulent kinetic energy dissipation rate and encourages similar analyses of existing data sets as finescale vertical profiles are much more widely measured than microstructure profiles. Mean profiles of dissipation are desirable because they allow for a parametrization of turbulent mixing and internal waves, necessary in ocean circulation models [Melet et al. (2013)] due to the different length and time scales of such phenomena.

Another microstructure data set, collected with a MR, was analyzed in a similar way. The depth integrated energy dissipation rate ϵ and the contribution of the smallest detectable mixing to the total energy dissipation were calculated for each one of the 130 vertical profiles. Unfortunately, the results do not seem to be comparable to those obtained from the VMP data. The systematic difference in the magnitude of the energy dissipation estimated with the two instruments suggests that there could be a bias in the calculation or comparison. Further processing is required to obtain two consistent data sets.

In conclusion, this work provides a broad overview of the microstructure data that were collected with the VMP during the SONNET expedition. This analysis of the turbulent energy dissipation southeast of the Walvis Ridge, at depths between approximately 100 and 1000 m, and on some of the available methods can be useful for further processing of these data or for future studies on the same topic and/on the same ocean region.

7   Acknowledgment

Appendices

A   Technical details

VMP Data Processing Information						
VMP Deployments	**Valid Profiles**	**coef0 Pressure**	**Number of T Probes**	**T_0**	**beta_1**	**beta_2**
3.1	2-3-4	-8.52	1	288.031	3049.28	$2.5 \cdot 10^5$
3.2	1-2-3	-8.57	1	288.080	3050.27	$2.6 \cdot 10^5$
3.3	1-2-3	-8.52	2	288.133	3050.76	$2.7 \cdot 10^5$
4.1	1-2-3	-8.57	2	288.207	3052.23	$2.7 \cdot 10^5$
5.1	1-2-3	-8.45	2	288.240	3054.29	$2.5 \cdot 10^5$
5.2	1-4	-8.57	1	288.23	3050.44	$2.3 \cdot 10^5$
5.3	1-2-3	-8.57	1	288.20	3050.95	$2.0 \cdot 10^5$
5.4	2-3-4	-8.51	1	288.192	3053.11	$1.9 \cdot 10^5$
14.1	1-2-6	-8.57	1	288.541	3051.50	$-8.1 \cdot 10^4$
15.1	1-2-3	-8.58	1	288.531	3050.83	$4.5 \cdot 10^5$
16.1	1-2-3	-8.63	1	288.557	3052.75	$2.2 \cdot 10^5$
20.1	1-2-3	-8.45	1	288.59	3054.01	$3.4 \cdot 10^5$
20.2	1-2-3	-8.57	1	288.579	3053.22	$2.7 \cdot 10^5$
21.2	1-2-3	-8.45	1	288.619	3050.55	$2.6 \cdot 10^5$
21.3	2-3-4	-8.45	1	288.670	3055.41	$2.1 \cdot 10^5$
22.1	2-3-4	-8.45	1	288.707	3051.37	$2.4 \cdot 10^5$
22.2	1-2-3	-8.63	1	288.722	3055.17	$2.2 \cdot 10^5$
23.1	1-2-3	-8.57	1	288.715	3051.65	$2.6 \cdot 10^5$
23.2	1-2-3	-8.57	1	288.738	3050.69	$2.3 \cdot 10^5$
28.1	1-2-3	-8.63	1	288.787	3053.79	$2.5 \cdot 10^5$
28.2	1-2-3	-8.52	1	288.778	3055.82	$2.7 \cdot 10^5$

Table 10: Processing parameters and data features for each VMP data file of the M180 SONNET expedition.

B List of results for the integration with depth of individual valid VMP profiles

The following pages contain a table that summarized the results obtained with the method described in the paragraph "Depth Integrated Dissipations ϵ" of Section 3.3.2 for individual valid profiles.

Block - Profile	ϵ_p $\cdot 10^{-4} \frac{W}{m^2}$	ϵ_b $\cdot 10^{-4} \frac{W}{m^2}$	$R_b = \epsilon_b/\epsilon_p$	ϵ_1 $\cdot 10^{-4} \frac{W}{m^2}$	$R_1 = \epsilon_1/\epsilon_p$	ϵ_2 $\cdot 10^{-4} \frac{W}{m^2}$	$R_2 = \epsilon_2/\epsilon_p$
3.1 - 2	7.3526	4.3120	0.59	0.60011	0.08	0.047042	0.01
3.1 - 3	4.2290	3.6166	0.86	0.18646	0.04	0.060734	0.01
3.1 - 4	4.5222	3.8240	0.85	0.22191	0.05	0.078158	0.02
3.2 - 1	5.0472	4.6643	0.92	0.25086	0.05	0.17455	0.03
3.2 - 2	5.5274	5.1777	0.94	0.23549	0.04	0.21938	0.04
3.2 - 3	5.5845	5.1696	0.93	0.25876	0.05	0.29668	0.05
3.3 - 1	5.1443	4.8139	0.94	0.44740	0.09	0.12115	0.02
3.3 - 2	5.7048	5.5963	0.98	0.14936	0.03	0.25202	0.04
3.3 - 3	5.9807	5.5640	0.93	0.17806	0.03	0.45814	0.08
4.1 - 1	7.1126	5.5213	0.78	1.1744	0.17	0.39313	0.06
4.1 - 2	6.3203	5.1663	0.82	0.74482	0.12	0.30324	0.05
4.1 - 3	6.4575	4.8831	0.76	1.3189	0.20	0.37158	0.06
5.1 - 1	5.5508	5.0196	0.90	0.24547	0.04	0.25407	0.05
5.1 - 2	6.5018	5.6926	0.88	0.25658	0.04	0.57217	0.09
5.1 - 3	5.9920	4.9020	0.82	0.88434	0.15	0.17924	0.03
5.2 - 1	6.1621	4.4840	0.73	1.1040	0.18	0.38998	0.06
5.2 - 4	4.8084	4.1938	0.87	0.55270	0.11	0.069349	0.01
5.3 - 1	7.4343	5.3275	0.72	1.9286	0.26	0.18435	0.02
5.3 - 2	5.0871	4.4336	0.87	0.24944	0.05	0.34665	0.07
5.3 - 3	5.8259	4.8821	0.84	0.56589	0.10	0.29079	0.05
5.4 - 2	5.6570	5.0826	0.90	0.42519	0.08	0.54827	0.10
5.4 - 3	5.6792	4.3482	0.77	0.93662	0.16	0.44979	0.08
5.4 - 4	5.3150	4.9287	0.93	0.30776	0.06	0.11521	0.02

Block - Profile	ϵ_p $\cdot 10^{-4} \frac{W}{m^2}$	ϵ_b $\cdot 10^{-4} \frac{W}{m^2}$	$R_b = \epsilon_b/\epsilon_p$	ϵ_1 $\cdot 10^{-4} \frac{W}{m^2}$	$R_1 = \epsilon_1/\epsilon_p$	ϵ_2 $\cdot 10^{-4} \frac{W}{m^2}$	$R_2 = \epsilon_2/\epsilon_p$
14.1 - 1	5.3544	4.0489	0.76	0.37514	0.07	0.42927	0.08
14.1 - 2	3.9589	3.0146	0.76	0.41093	0.10	0.24165	0.6
14.1 - 6	3.4981	2.6014	0.74	0.19763	0.06	0.27443	0.08
15.1 - 1	3.1712	2.5633	0.80	0.25341	0.08	0.21944	0.07
15.1 - 2	2.4832	2.0342	0.82	0.10772	0.04	0.17990	0.07
15.1 - 3	3.5733	2.9872	0.84	0.29535	0.08	0.087088	0.02
16.1 - 1	4.9424	3.7704	0.76	0.74654	0.15	0.41877	0.08
16.1 - 2	5.2825	3.3295	0.63	1.3465	0.25	0.56538	0.11
16.1 - 3	6.0150	3.6277	0.60	0.97506	0.16	0.49923	0.08
20.1 - 1	4.4980	4.2821	0.95	0.27930	0.06	0.19434	0.04
20.1 - 2	4.2514	3.5396	0.83	0.45886	0.11	0.19365	0.05
20.1 - 3	4.4286	3.2445	0.73	0.19348	0.04	0.88823	0.20
20.2 - 1	2.9835	2.3236	0.78	0.10963	0.04	0.13443	0.05
20.2 - 2	3.8020	3.1749	0.84	0.16831	0.04	0.16520	0.04
20.2 - 3	3.6971	3.4521	0.93	0.059777	0.02	0.22061	0.06
21.2 - 1	4.8330	4.0294	0.83	0.76541	0.16	0.13215	0.03
21.2 - 2	3.8074	3.6038	0.95	0.092797	0.02	0.085890	0.02
21.2 - 3	4.1855	3.6759	0.88	0.078662	0.02	0.053443	0.01
21.3 - 2	4.6826	4.2955	0.92	0.10425	0.02	0.094769	0.02
21.3 - 3	4.3576	4.1655	0.96	0.13279	0.03	0.076704	0.02
21.3 - 4	4.5618	4.2833	0.94	0.24904	0.05	0.075078	0.02
22.1 - 2	4.3055	3.3920	0.79	0.62314	0.14	0.15180	0.04
22.1 - 3	4.4460	3.3013	0.74	0.11990	0.03	0.38512	0.09
22.1 - 4	3.5155	3.0525	0.87	0.32126	0.09	0.13089	0.04
22.2 - 1	3.7700	3.5616	0.94	0.11730	0.03	0.12142	0.03
22.2 - 2	4.4539	3.4512	0.77	0.10648	0.02	0.74763	0.17
22.2 - 3	4.4637	3.9922	0.89	0.13578	0.03	0.24761	0.06

Block - Profile	ϵ_p $\cdot 10^{-4} \frac{W}{m^2}$	ϵ_b $\cdot 10^{-4} \frac{W}{m^2}$	$R_b =$ ϵ_b/ϵ_p	ϵ_1 $\cdot 10^{-4} \frac{W}{m^2}$	$R_1 =$ ϵ_1/ϵ_p	ϵ_2 $\cdot 10^{-4} \frac{W}{m^2}$	$R_2 =$ ϵ_2/ϵ_p
23.1 - 1	4.7373	3.9555	0.84	0.28442	0.06	0.05621	0.01
23.1 - 2	3.7278	3.2993	0.89	0.11390	0.03	0.18327	0.05
23.1 - 3	4.1881	3.7783	0.90	0.18263	0.04	0.090065	0.02
23.2 - 1	4.2867	4.0420	0.94	0.12172	0.03	0.051840	0.03
23.2 - 2	3.8335	3.4170	0.89	0.28903	0.08	0.092598	0.02
23.2 - 3	3.6250	3.2732	0.90	0.066639	0.02	0.079839	0.02
28.1 - 1	3.8724	2.9633	0.77	0.62189	0.16	0.079664	0.02
28.1 - 2	3.2185	2.9656	0.92	0.091664	0.03	0.035020	0.01
28.1 - 3	4.5140	3.6000	0.80	0.85499	0.19	0.10709	0.02
28.2 - 1	5.2074	4.2343	0.81	0.34992	0.07	0.084826	0.02
28.2 - 2	4.5856	4.0741	0.89	0.25148	0.05	0.13103	0.03
28.2 - 3	4.6854	4.1637	0.89	0.62917	0.13	0.13804	0.03
Mean			0.84		0.08		0.06
SD			0.09		0.06		0.07

Table 11: List of valid profiles with their depth integrated energy dissipation rate ϵ_p between 100 and 600 m. For each profile a dissipation background curve between 100 and 600 m is obtained and integrated. This depth integrated energy dissipation rate is called ϵ_b. The ratio $R_b = \epsilon_b/\epsilon_p$ can be seen as the percentage contribution of the background dissipation to the total dissipation curve of that profile. ϵ_1 and ϵ_2 correspond to the depth integrated energy dissipation rate of two outstanding turbulent events in the considered profile, the first one between 100 and 300 m and the second one between 300 and 600. The ratios $R_1 = \epsilon_1/\epsilon_p$ and $R_2 = \epsilon_2/\epsilon_p$ can be seen as the percentage contributions of each one of the two dissipative events to the total dissipation curve of that profile. The mean contribution and the standard deviation of the background curve, the turbulent event between 100 and 300 m, and the turbulent event between 300 and 600, respectively, are also calculated.

C   Table for Thorpe Scale calculation

Deployment	Profile	P start (dbar)	δ_D (kg m^{-3})
3.1	4	11.5	0.0029
3.3	1	12.8	0.0020
5.1	1	17.9	0.0014
5.2	4	12.3	0.0029
14.1	1	18.4	0.0020
15.1	2	21	0.0026
20.2	2	71.4	0.0026
21.3	3	17.9	0.0019
22.2	2	11.4	0.0024
23.1	2	269.2	0.0060
28.2	3	52.4	0.0032
Mean	-	-	**0.0027**

Table 12: Layers (1 dbar thick) that are well mixed in density and that were used to calculate the standard deviation of density. The mean over all layers was used as threshold level for identifying density inversion in the density profiles.

D List of MR profiles and their depth-integrals

Prof N	Lat (°S)	Lon (°E)	Start Time	End Time	$\epsilon \cdot 10^{-5}$ $(\frac{W}{m^{-2}})$	$\delta_\epsilon \cdot 10^{-10}$ $(\frac{W}{m^{-2}})$
1	36.935	6.937	16.3.22 02:16:21	16.3.2203:43:14	3.00708	1
2	36.954	6.936	16.3.22 03:43:33	16.3.22 04:59:50	3.86788	2
3	36.982	6.933	16.3.22 06:40:47	16.3.22 07:57:47	3.10728	1
4	36.999	6.918	16.3.22 08:51:26	16.3.22 10:20:50	4.53308	2
5	37.031	6.913	16.3.22 11:54:06	16.3.22 10:21:02	3.76389	2
6	37.020	6.914	16.3.22 10:21:08	16.3.22 11:37:43	3.77088	2
7	37.052	6.909	16.3.22 13:19:42	16.3.22 14:35:54	3.02946	1
8	37.068	6.897	16.3.22 15:15:49	16.3.22 16:44:07	3.91028	3
9	37.097	6.895	16.3.22 18:20:36	16.3.22 19:42:47	4.32218	4
10	37.087	6.896	16.3.22 16:44:22	16.3.22 18:04:28	3.88047	3
11	37.116	6.894	16.3.22 19:43:01	16.3.22 02:16:21	5.12966	2
12	36.935	6.937	16.3.22 02:16:27	16.3.22 03:43:14	3.00708	1
13	37.117	6.894	16.3.22 19:43:01	16.3.22 21:37:41	5.06468	2
14	37.132	6.886	16.3.22 21:37:47	16.3.22 23:02:35	2.62690	1
15	37.156	6.883	17.3.22 00:36:43	17.3.22 02:02:13	12.7002	10
16	37.148	6.884	16.3.22 23:02:49	17.3.22 00:20:18	4.13396	5
17	37.170	6.881	17.3.22 02:02:29	16.3.22 02:16:21	4.40421	3
18	37.184	6.875	17.3.22 04:00:42	17.3.22 05:23:30	5.49702	3
19	37.209	6.868	17.3.22 06:53:44	17.3.22 08:13:50	4.41838	4
20	37.201	6.870	17.3.22 05:23:42	17.3.22 06:38:12	3.79703	2
21	37.227	6.864	17.3.22 08:14:02	17.3.22 09:33:56	3.84484	2
22	37.272	6.850	17.3.22 16:32:38	17.3.22 18:00:14	2.78429	1
23	37.283	6.847	17.3.22 19:32:16	17.3.22 18:00:31	3.46843	1
24	37.279	6.848	17.3.22 18:00:37	17.3.22 19:16:49	4.64084	2
25	37.288	6.847	17.3.22 20:51:12	16.3.22 02:16:21	2.69143	1
26	37.321	6.831	18.3.22 04:53:36	18.3.22 06:17:41	3.96772	2
27	37.329	6.834	18.3.22 07:51:14	18.3.22 09:14:43	3.54751	2

Prof N	Lat (°S)	Lon (°E)	Start Time	End Time	$\epsilon \cdot 10^{-5}$ $(\frac{W}{m^{-2}})$	$\delta_\epsilon \cdot 10^{-10}$ $(\frac{W}{m^{-2}})$
26	37.321	6.831	18.3.22 04:53:36	18.3.22 06:17:41	3.96772	2
27	37.329	6.834	18.3.22 07:51:14	18.3.22 09:14:43	3.54751	2
28	37.326	6.833	18.3.22 06:17:56	18.3.22 07:34:13	4.06768	2
29	37.333	6.836	18.3.22 09:14:56	16.3.22 02:16:21	4.47597	2
30	37.341	6.827	18.3.22 11:12:43	18.3.22 12:39:37	3.00198	1
31	37.342	6.829	18.3.22 14:12:01	18.3.22 15:35:19	3.59026	2
32	37.342	6.828	18.3.22 12:39:53	18.3.22 13:55:46	2.00249	1
33	37.344	6.830	18.3.22 15:35:33	18.3.22 16:52:08	2.70274	1
34	37.348	6.827	18.3.22 17:21:16	18.3.22 18:46:58	3.63253	3
35	37.369	6.827	18.3.22 20:19:27	18.3.22 18:47:13	3.84635	3
36	37.362	6.827	18.3.22 18:47:19	18.3.22 20:03:25	7.44537	9
37	37.382	6.827	18.3.22 21:39:53	18.3.22 22:54:59	17.05607	8
38	37.391	6.819	18.3.22 23:43:11	19.3.22 01:07:53	2.27289	1
39	37.404	6.827	19.3.22 02:41:21	19.3.22 01:08:05	3.86486	3
40	37.399	6.824	19.3.22 01:08:11	19.3.22 02:24:59	3.90161	2
41	37.412	6.832	19.3.22 04:01:25	19.3.22 05:17:55	4.28524	4
42	37.417	6.829	19.3.22 05:57:45	19.3.22 07:25:02	4.31963	3
43	37.425	6.834	19.3.22 08:57:07	19.3.22 10:17:01	2.75279	1
44	37.422	6.832	19.3.22 07:25:17	19.3.22 08:41:11	2.91907	1
45	37.429	6.838	19.3.22 10:17:17	16.3.22 02:16:21	2.53722	1
46	37.435	6.835	19.3.22 12:12:04	19.3.22 13:32:45	3.05140	2
47	37.446	6.839	19.3.22 15:05:44	19.3.22 16:28:25	2.80983	1
48	37.442	6.837	19.3.22 13:33:02	19.3.22 14:49:20	2.24202	1
49	37.453	6.841	19.3.22 16:28:42	19.3.22 17:43:48	3.53193	2
50	37.456	6.837	19.3.22 18:22:53	19.3.22 19:49:10	2.72503	1
51	37.465	6.846	19.3.22 21:23:59	19.3.22 19:49:25	6.50450	5
52	37.462	6.843	19.3.22 19:49:31	19.3.22 21:08:00	3.17190	1
53	37.468	6.852	19.3.22 22:47:45	16.3.22 02:16:21	3.51872	1
54	37.470	6.852	19.3.22 22:47:45	20.3.22 00:43:02	3.51750	1
55	37.473	6.849	20.3.22 00:43:08	20.3.22 02:07:32	3.29738	2

Prof N	Lat (°S)	Lon (°E)	Start Time	End Time	$\epsilon \cdot 10^{-5}$ ($\frac{W}{m^{-2}}$)	$\delta_\epsilon \cdot 10^{-10}$ ($\frac{W}{m^{-2}}$)
56	37.475	6.856	20.3.22 03:40:51	20.3.22 05:03:33	5.58443	3
57	37.474	6.853	20.3.22 02:07:51	20.3.22 03:24:21	4.34274	4
58	37.475	6.861	20.3.22 05:03:51	16.3.22 02:16:21	11.51122	9
59	37.476	6.861	20.3.22 05:03:51	20.3.22 07:01:55	11.51237	9
60	37.480	6.857	20.3.22 07:02:01	20.3.22 08:28:18	7.37326	6
61	37.485	6.859	20.3.22 10:00:19	20.3.22 08:28:33	3.77533	2
62	37.483	6.858	20.3.22 08:28:39	20.3.22 09:44:03	8.02245	9
63	37.489	6.861	20.3.22 11:23:53	20.3.22 12:40:10	5.17200	6
64	37.491	6.857	20.3.22 13:21:48	20.3.22 14:47:47	3.85937	2
63	37.489	6.861	20.3.22 11:23:53	20.3.22 12:40:10	5.17200	6
64	37.491	6.857	20.3.22 13:21:48	20.3.22 14:47:47	3.85937	2
65	37.496	6.864	20.3.22 16:20:49	20.3.22 17:44:24	4.36794	2
66	37.494	6.862	20.3.22 14:48:01	20.3.22 16:04:49	3.94137	2
67	37.498	6.869	20.3.22 17:44:41	16.3.22 02:16:21	15.9899	20
68	37.501	6.866	20.3.22 19:38:19	20.3.22 21:04:00	2.94874	1
69	37.502	6.872	20.3.22 22:36:09	20.3.22 23:59:21	7.33070	5
70	37.502	6.870	20.3.22 21:04:15	20.3.22 22:20:02	17.8245	10
71	37.500	6.877	20.3.22 23:59:35	16.3.22 02:16:21	4.78371	2
72	37.502	6.876	20.3.22 23:59:35	21.3.22 01:57:42	4.78255	2
73	37.506	6.873	21.3.22 01:57:48	21.3.22 03:22:30	5.57928	4
74	37.520	6.878	21.3.22 04:55:30	21.3.22 06:14:53	4.92044	3
75	37.515	6.876	21.3.22 03:22:46	21.3.22 04:39:46	6.38791	4
76	37.527	6.881	21.3.22 06:15:06	16.3.22 02:16:21	4.73869	3
77	37.529	6.881	21.3.22 06:15:06	21.3.22 08:07:46	4.73866	3
78	37.535	6.880	21.3.22 08:07:52	21.3.22 09:32:46	7.46794	8
79	37.545	6.890	21.3.22 11:05:10	21.3.22 09:33:00	8.86981	6
80	37.541	6.886	21.3.22 09:33:06	21.3.22 10:48:54	4.39257	2
81	37.549	6.897	21.3.22 12:26:20	16.3.22 02:16:21	6.73485	5
82	37.551	6.897	21.3.22 12:26:20	21.3.22 14:14:53	6.72916	5
83	37.554	6.900	21.3.22 14:14:59	21.3.22 15:40:35	16.2503	20

Prof N	Lat (°S)	Lon (°E)	Start Time	End Time	$\epsilon \cdot 10^{-5}$ ($\frac{W}{m^{-2}}$)	$\delta_\epsilon \cdot 10^{-10}$ ($\frac{W}{m^{-2}}$)
84	37.560	6.914	21.3.22 17:13:57	21.3.22 15:40:49	13.94438	9
85	37.558	6.909	21.3.22 15:40:55	21.3.22 16:57:19	6.73162	3
86	37.560	6.924	21.3.22 18:37:09	16.3.22 02:16:21	10.59529	5
87	37.563	6.923	21.3.22 18:37:09	21.3.22 20:23:19	10.60500	5
88	37.568	6.925	21.3.22 20:23:25	21.3.22 21:48:30	11.24365	7
87	37.563	6.923	21.3.22 18:37:09	21.3.22 20:23:19	10.60500	5
88	37.568	6.925	21.3.22 20:23:25	21.3.22 21:48:30	11.24365	7
89	37.590	6.927	21.3.22 23:20:33	21.3.22 21:48:48	7.69024	4
90	37.582	6.926	21.3.22 21:48:54	21.3.22 23:04:05	8.74081	6
91	37.605	6.929	22.3.22 00:44:07	22.3.22 02:01:24	4.38137	3
92	37.613	6.929	22.3.22 02:46:06	22.3.22 04:11:59	5.15438	2
93	37.634	6.939	22.3.22 05:43:50	22.3.22 04:12:14	3.17877	1
94	37.626	6.935	22.3.22 04:12:20	22.3.22 05:27:43	6.52730	6
95	37.644	6.945	22.3.22 07:06:35	16.3.22 02:16:21	4.13599	2
96	37.650	6.952	22.3.22 09:06:16	22.3.22 10:35:03	3.13315	2
97	37.653	6.968	22.3.22 12:07:27	22.3.22 10:35:19	4.61290	3
98	37.652	6.963	22.3.22 10:35:25	22.3.22 11:51:19	4.26344	2
99	37.655	6.979	22.3.22 13:30:19	22.3.22 14:50:49	5.28785	3
100	37.652	6.987	22.3.22 15:30:59	22.3.22 16:55:59	4.65499	2
101	37.649	7.015	22.3.22 18:28:03	22.3.22 16:56:19	10.32234	6
102	37.650	7.005	22.3.22 16:56:25	22.3.22 18:12:19	14.3401	10
103	37.645	7.031	22.3.22 19:48:59	16.3.22 02:16:21	3.51693	1
104	37.647	7.032	22.3.22 19:48:59	22.3.22 21:41:15	3.51649	1
105	37.643	7.042	22.3.22 21:41:21	22.3.22 23:04:15	3.48982	2
106	37.642	7.067	23.3.22 00:35:45	23.3.22 01:55:02	3.13364	2
107	37.642	7.058	22.3.22 23:04:36	23.3.22 00:19:53	3.65866	3
108	37.639	7.082	23.3.22 01:55:15	16.3.22 02:16:21	3.50869	2
109	37.641	7.083	23.3.22 01:55:15	23.3.22 03:48:47	3.51123	2
110	37.638	7.094	23.3.22 03:48:53	23.3.22 05:14:10	3.59095	2
111	37.634	7.123	23.3.22 06:44:55	23.3.22 08:06:55	3.18961	2

Prof N	Lat (°S)	Lon (°E)	Start Time	End Time	$\epsilon \cdot 10^{-5}$ ($\frac{W}{m^{-2}}$)	$\delta_\epsilon \cdot 10^{-10}$ ($\frac{W}{m^{-2}}$)
112	37.635	7.112	23.3.22 05:14:27	23.3.22 06:29:03	3.01339	2
113	37.632	7.141	23.3.22 08:07:07	23.3.22 09:24:55	2.27897	1
114	37.626	7.152	23.3.22 10:03:17	23.3.22 11:27:46	2.89954	1
115	37.623	7.175	23.3.22 12:59:19	23.3.22 11:28:03	6.54651	3
116	37.624	7.167	23.3.22 11:28:09	23.3.22 12:43:09	9.88351	10
117	37.621	7.190	23.3.22 14:24:03	23.3.22 15:40:26	2.87405	2
118	37.614	7.200	23.3.22 16:17:02	23.3.22 17:42:43	7.37985	4
119	37.612	7.224	23.3.22 19:14:06	23.3.22 20:34:00	5.41709	2
120	37.613	7.216	23.3.22 17:42:56	23.3.22 18:58:25	12.8998	20
121	37.608	7.238	23.3.22 20:34:16	16.3.22 02:16:21	3.34049	2
122	37.607	7.245	23.3.22 22:28:59	23.3.22 23:51:41	3.96379	2
123	37.607	7.269	24.3.22 01:21:31	23.3.22 23:51:55	6.60482	4
124	37.607	7.261	23.3.22 23:52:01	24.3.22 01:05:55	11.28722	9
125	37.605	7.284	24.3.22 02:43:35	16.3.22 02:16:21	6.83219	8
126	37.603	7.293	24.3.22 04:37:01	24.3.22 06:05:31	11.18417	8
127	37.604	7.315	24.3.22 07:36:28	24.3.22 08:58:09	6.66607	2
128	37.604	7.307	24.3.22 06:05:46	24.3.22 07:20:39	5.03515	3
129	37.605	7.329	24.3.22 08:58:26	24.3.22 10:13:13	4.86046	3

Table 13: List of profiles measured by the MR and corresponding geographic coordinates (calculated as mean latitude and longitude), start and end time of the profile, and depth integrated energy dissipation rate (ϵ) with uncertainty (δ_ϵ)

Bibliography

Brown, E., Colling, A., Park, D., Phillips, J., Rothery, D., and Wright, J. (2001). Ocean Circulation (Second Edition). Butterworth-Heinemann, Oxford.

Dillon, T. M. (1982). Vertical overturns: A comparison of Thorpe and Ozmidov length scales. *Journal of Geophysical Research*, 87:9601–9613.

Douglas, W., Lueck, R., and McMillan, J. (2020). *ODAS MATLAB Library, Technical Manual, Version 4.4*. Rockland Scientific International Inc.

Eden, C., Czeschel, L., and Olbers, D. (2014). Toward Energetically Consistent Ocean Models. *Journal of Physical Oceanography*, 44(12):3160 – 3184.

Ferron, B., Mercier, H., Speer, K., Gargett, A., and Polzin, K. (1998). Mixing in the Romanche Fracture Zone. *J. Phys. Oceanogr.*, 28:1929–1945.

Gargett, A. and Garner, T. (2008). Determining Thorpe Scales from Ship-Lowered CTD Density Profiles. *Journal of Atmospheric and Oceanic Technology*, 25(9):1657–1670.

Gregg, M., D'Asaro, E., Riley, J., and Kunze, E. (2018). Mixing Efficiency in the Ocean. *Annual Review of Marine Science*, 10(1):443–473.

Gregg, M. C. (1987). Diapycnal mixing in the thermocline: A review. *Journal of Geophysical Research*, 92:5249–5286.

Gregg, M. C. (1989). Scaling turbulent dissipation in the thermocline. *Journal of Geophysical Research: Oceans*, 94(C7):9686–9698.

Gregg, M. C. (2021). *Ocean Mixing*. Cambridge University Press.

Gregg, M. C. and Sanford, T. B. (1988). The dependence of turbulent dissipation on stratification in a diffusively stable thermocline. *Journal of Geophysical Research: Oceans*, 93(C10):12381–12392.

Lien, R.-C. and Gregg, M. C. (2001). Observations of turbulence in a tidal beam and across a coastal ridge, journal = Journal of Geophysical Research: Oceans. 106(C3):4575–4591.

Lueck, R. (2016). *Calculating the Rate of Dissipation of Turbulent Kinetic Energy, RSI Technical Note 28*. Rockland Scientific International Inc.

Lueck, R., Murowinski, E., and McMillan, J. (2020). *A Guide to Data Processing, (ODAS Matlab Library Version 4.4), RSI Technical Note 39*. Rockland Scientific International Inc.

Mater, B. D., Venayagamoorthy, S. K., Laurent, L. S., and Moum, J. N. (2015). Biases in Thorpe-Scale Estimates of Turbulence Dissipation. Part I: Assessments from Large-Scale Overturns in Oceanographic Data. *Journal of Physical Oceanography*, 45(10):2497 – 2521.

McDougall, T. and Barker, P. (2011). Getting started with TEOS-10 and the Gibbs Seawater (GSW) Oceanographic Toolbox. SCOR/IAPSO Working Group 127, ISBN 978-0-646-55621-5.

Melet, A., Hallberg, R., Legg, S., and Polzin, K. (2013). Sensitivity of the Ocean State to the Vertical Distribution of Internal-Tide-Driven Mixing. *Journal of Physical Oceanography*, 43(3):602 – 615.

Munk, W. and Wunsch, C. (1998). Abyssal recipes II: energetics of tidal and wind mixing. *Deep Sea Research Part I: Oceanographic Research Papers*, 45(12):1977–2010.

Munk, W. H. (1966). Abyssal recipes. *Deep Sea Research and Oceanographic Abstracts*, 13(4):707–730.

Munk, W. H. (1981). *Internal Waves and Small-Scale Processes*, book section 9, pages 264–298. The MIT Press, Boston, MA.

Ozmidov, R. (1965). On the turbulent exchange in a stably stratified ocean (English translation). *Izv. Acad. Sci. USSR Atmos. Oceanic Phys.*, 1:853–860.

Polzin, K. L., Toole, J. M., Ledwell, J. R., and Schmitt, R. W. (1997). Spatial Variability of Turbulent Mixing in the Abyssal Ocean. *Science*, 276(5309):93–96.

Richardson, P. L. (2007). Agulhas leakage into the Atlantic estimated with subsurface floats and surface drifters. *Deep Sea Research Part I: Oceanographic Research Papers*, 54(8):1361–1389.

Rockland (2021). *User Manual, VMP-250-IR, PN 010-151-20, Revision 1.2*. Rockland Scientific International Inc.

Schultze, L. K. P., Merckelbach, L. M., and Carpenter, J. R. (2017). Turbulence and Mixing in a Shallow Shelf Sea From Underwater Gliders. *Journal of Geophysical Research: Oceans*, 122(11):9092–9109.

Smith, J. (2019). A Comparison of Two Methods Using Thorpe-Sorting to Estimate Mixing. *Journal of Atmospheric and Oceanic Technology*, 37.

Stansfield, K., Garrett, C., and Dewey, R. (2001). The Probability Distribution of the Thorpe Displacement within Overturns in Juan de Fuca Strait. *Journal of Physical Oceanography*, 31(12):3421 – 3434.

Sugiura, N., Kouketsu, S., Masuda, S., Osafune, S., and Yasuda, I. (2018). Estimating vertically averaged energy dissipation rate. The preprint has been withdrawn by the authors. *Nonlinear Processes in Geophysics. Discussions*, pages 1–23.

Talley, L., Pickard, G., Emery, W., and Swift, J. (2011). *Descriptive physical oceanography: An introduction: Sixth edition*, pages 1–555.

Teledyne (2017). *Slocum G3 Glider Operators Manual, Version 4.4*. Teledyne Instruments, Inc.

Thorpe, S. A. (1977). Turbulence and mixing in a Scottish Loch. *Philosophical Transactions of the Royal Society of London. Series A, Mathematical and Physical Sciences*, 286(1334):125–181.

Wright, J., Colling, A., and Par, D. (1999). Waves, Tides and Shallow-Water Processes (Second Edition). Open University Oceanography. Butterworth-Heinemann, Oxford.

Offizielle Erklärungen von

Name: _____ Matrikelnr.: _____

Eigenständigkeitserklärung

Ich versichere, dass ich die vorliegende Arbeit selbstständig verfasst und keine anderen als die angegebenen Quellen und Hilfsmittel verwendet habe.

Alle Teile meiner Arbeit, die wortwörtlich oder dem Sinn nach anderen Werken entnommen sind, wurden unter Angabe der Quelle kenntlich gemacht. Gleiches gilt auch für Zeichnungen, Skizzen, bildliche Darstellungen sowie für Quellen aus dem Internet.

Die Arbeit wurde in gleicher oder ähnlicher Form noch nicht als Prüfungsleistung eingereicht.

Die elektronische Fassung der Arbeit stimmt mit der gedruckten Version überein.

Mir ist bewusst, dass wahrheitswidrige Angaben als Täuschung behandelt werden.

A) Erklärung zur Veröffentlichung von Bachelor- oder Masterarbeiten

Die Abschlussarbeit wird zwei Jahre nach Studienabschluss dem Archiv der Universität Bremen zur dauerhaften Archivierung angeboten. Archiviert werden:
1) Masterarbeiten mit lokalem oder regionalem Bezug sowie pro Studienfach und Studienjahr 10 % aller Abschlussarbeiten
2) Bachelorarbeiten des jeweils ersten und letzten Bachelorabschlusses pro Studienfach u. Jahr.

Ich bin damit einverstanden, dass meine Abschlussarbeit im Universitätsarchiv für wissenschaftliche Zwecke von Dritten eingesehen werden darf.

Ich bin damit einverstanden, dass meine Abschlussarbeit nach 30 Jahren (gem. §7 Abs. 2 BremArchivG) im Universitätsarchiv für wissenschaftliche Zwecke von Dritten eingesehen werden darf.

Ich bin nicht damit einverstanden, dass meine Abschlussarbeit im Universitätsarchiv für wissenschaftliche Zwecke von Dritten eingesehen werden darf.

B) Einverständniserklärung über die Bereitstellung und Nutzung der Bachelorarbeit / Masterarbeit / Hausarbeit in elektronischer Form zur Überprüfung durch Plagiatssoftware

Eingereichte Arbeiten können mit der Software *Plagscan* auf einem hauseigenen Server auf Übereinstimmung mit externen Quellen und der institutionseigenen Datenbank untersucht werden.

Zum Zweck des Abgleichs mit zukünftig zu überprüfenden Studien- und Prüfungsarbeiten kann die Arbeit dauerhaft in der institutionseigenen Datenbank der Universität Bremen gespeichert werden.

Ich bin damit einverstanden, dass die von mir vorgelegte und verfasste Arbeit zum Zweck der Überprüfung auf Plagiate auf den *Plagscan*-Server der Universität Bremen hochgeladen wird.

Ich bin ebenfalls damit einverstanden, dass die von mir vorgelegte und verfasste Arbeit zum o.g. Zweck auf dem *Plagscan*-Server der Universität Bremen hochgeladen u. dauerhaft auf dem *Plagscan*-Server gespeichert wird.

Ich bin nicht damit einverstanden, dass die von mir vorgelegte u. verfasste Arbeit zum o.g. Zweck auf dem *Plagscan*-Server der Universität Bremen hochgeladen u. dauerhaft gespeichert wird.

Mit meiner Unterschrift versichere ich, dass ich die obenstehenden Erklärungen gelesen und verstanden habe. Mit meiner Unterschrift bestätige ich die Richtigkeit der oben gemachten Angaben.

_____   _____
Datum, Ort   Unterschrift